Dramatic HER Suppression on Ag Electrodes via Molecular Films for Highly Selective CO_2 to CO Reduction

Arnaud Thevenon[‡], Alonso Rosas-Hernandez[‡], Alex M. Fontani Herreros, Theodor Agapie* and Jonas C. Peters*

Joint Center for Artificial Photosynthesis (JCAP) and Division of Chemistry and Chemical Engineering, California Institute of Technology (Caltech), Pasadena, California 91125, United States

[‡]The authors contributed equally to this work.

Table of Contents

Materials and Methods 3
Electrochemical Measurements 3
Electrochemical Active surface Area (ECSA) and Partial Current Density Experiments 4
X-ray Photoelectron Spectroscopy (XPS) 5
Atomic Force Microscopy (AFM) 5
Scanning Electron Microscopy (SEM) and Energy Dispersive Spectroscopy (EDS) 5
Physical Vapor Deposited Silver Electrode Preparation (PVD) 5
Supporting Figures and Tables 6
Table S1. Faradaic Efficiencies (FEs) for CO_2RR products and H_2 on Ag at different potential. 6
Fig. S1. (a) FEs; (b) current densities for CO_2RR products and H_2 on Ag at different potential. 7
Table S2. FEs for CO_2RR products and H_2 on **Ag-1** at different potential. 8
Fig. S2. (a) FEs; (b) CO_2RR products and H_2 current densities on **Ag-1** at different potential. 9
Table S3. FEs for CO_2RR products and H_2 on **Ag-2** at different potential. 10
Fig. S3. (a) FEs; (b) CO_2RR products and H_2 current densities on **Ag-2** at different potential. 11
Table S4. FEs for CO_2RR products and H_2 on **Ag-1** and **Ag-2** with an additive free electrolyte. 12
Table S5. FEs for CO_2RR products and H_2 on **Ag-1** at different pH at –1.1 V. 12
Fig. S4. XPS of Ag, **Ag-1** and **Ag-2**. 13
Fig. S5. ^{1}H NMR spectrum of the film extracted form **Ag-2**. 14
Fig. S6. ^{1}H-^{1}H COSY NMR spectrum of the film extracted from **Ag-2**. 14
Fig. S7. ^{1}H NMR spectra of the film extracted from **Ag-2**, **Cu-2** and from the reduction of **2-Cl**. 15
Fig. S8. ^{1}H NMR spectrum of the film extracted from **Ag-1**. 16
Fig. S9. ^{1}H-^{1}H COSY NMR spectrum of the film extracted from **Ag-1**. 16
Fig. S10. Stack of ^{1}H NMR spectra of the film extracted from **Ag-1** and **Cu-1**. 17
Fig. S11. ESI-MS spectrum of the film extracted from **Ag-1**. 18
Fig. S12. *Ex-situ* SEM images of bare Ag before and after bulk electrocatalysis. 20
Fig. S13. *Ex-situ* SEM images of **Ag-1** before and after extracting the organic film. 20
Fig. S14. *Ex-situ* SEM images of **Ag-1** after 1 h of bulk electrocatalysis at –1.4 V. 20
Fig. S15. *Ex-situ* AFM images of bare Ag, **Ag-1** and **Ag-2** before and after electrocatalysis. 21
Fig. S16. Full Tafel plot. 22
Fig. S17. Examples of voltammograms at different scan rates between –0.1 V and –0.2 V. 23
Table S6. Cathodic and anodic currents recorded by CVs at different scan rates for Ag. 23
Table S7. Cathodic and anodic currents recorded by CVs at different scan rates for **Ag-2**. 24
Fig. S18. Example of plot showing the experimentally determined ECSA for Ag and **Ag-2**. 24
Fig. S19. Plot of normalized j_{H2} and j_{CO} at –0.9 V for different electrodeposition time of **2-Cl**. 25
Table S8. Summary of data for ECSA and j_{H2} at –0.9 V at different electrodeposition time. 26
Table S9. Summary of data for ECSA and j_{CO} at –0.9 V at different electrodeposition time. 26
Fig. S20. LSV scans in N_2-saturated electrolyte. 27
Fig. S21. LSV scans in CO_2-saturated electrolyte. 27
Fig. S22. Plot of the dependence of the rotation rate of the Ag electrode and j_{H2}. 28
Fig. S23. Kutecky-Levich plot of j_{H2}. 28
Fig. S24. $p$$CO_2$ dependence of j_{CO} at –1.1 V. 29
Fig. S25. $p$$CO_2$ dependence of j_{CO} at –0.9 V (a) before, (b) after correction with ECSA. 29
Fig. S26. Voltamogram of Ag in CO_2-saturated 0.1 M $KHCO_3$ electrolyte. 30
Fig. S27. Voltamogram of Ag in CO_2-saturated 0.1 M $KHCO_3$ electrolyte with **1-Br$_2$**. 30
Fig. S28. Voltamogram of Ag in CO_2-saturated 0.1 M $KHCO_3$ electrolyte with **2-Cl**. 30
Fig. S29. Plot of the ECSA against the electrodeposition time under N_2. 31
Fig. S30. Plot of the j_{H2} at –1.1 V against the electrodeposition time under N_2. 32
Table S10. Summary of data for ECSA and j_{H2} at –1.1 V against the electrodeposition time. 32
Table S11. Summary of data for ECSA and j_{CO} at –1.1 V against the electrodeposition time. 33
Fig. S31. Plot of the ECSA against the electrodeposition time under CO_2. 33
Fig. S32. Plost of j_{CO} at –1.1 V and the electrodeposition time under CO_2. 34
Fig. S33. Evolution of FEs for CO and H_2, and total current density over 24 h. 34
References. 35

Materials and Methods

All solvents and reagents were obtained from commercial sources (Aldrich and Merck) and used as received, unless stated otherwise. The N,N'-ethyl-1,10-phenanthrolinium dibromide (phenanthrolinium, **1-Br$_2$**) and tolyl-pyridinium chloride (**2-Cl**) additives were synthesized according to previous literature procedures (1, 2) and recrystallized from MeOH/Ether (1:5) prior to use. Silver foil (99.998% Ag, 25 mm × 25 mm × 0.1 mm) were purchased from Alfa Aesar and the potassium carbonate (99.995%) from Sigma-Aldrich. Natural abundance CO_2 (Research grade) was purchased from Airgas. Deuterium dioxide (D 99.96%), d-chloroform (D 99.8%) and d_6-dimethylsulfoxide (D 99.8%) were purchased from Cambridge Isotope Laboratories. Water was purified by a Nanopure Analytical Ultrapure Water System (Thermo Scientific) or a Milli-Q Advantage A10 Water Purification System (Millipore) with specific resistance of 18.2 MΩ·cm at 25 °C. ^{1}H and ^{13}C NMR spectra were recorded on a Bruker 400 MHz instrument with a prodigy broadband cryoprobe. Shifts were reported relative to the residual solvent peak. Upon receiving, silver foil was polished to a mirror-like finish using alumina paste (0.05 μm, Buehler) followed by rinsing and sonicating in water to remove residual alumina. Before each experiment, the silver foil was manually polished using alumina paste (0.05 μm, Buehler), rinsed with 500 mL of ultra-pure water, sonicated for 5 min in ultra-purewater, subsequently washed with 500 mL of ultra-pure water and dried under a stream of nitrogen gas. Potassium bicarbonate electrolyte ($KHCO_3$(aq), 0.1 M) was prepared by sparging an aqueous solution of potassium carbonate (K_2CO_3(aq), 0.05 M) with CO_2 for at least 1 hour prior to electrolysis. This process converts K_2CO_3 into $KHCO_3$ and saturates the electrolyte solution with CO_2. The proper organic salt additive was added to the 0.1 M $KHCO_3$(aq) catholyte (unless otherwise stated [additive] = 10 mM) whereas 0.1 M $KHCO_3$(aq) without any additives was used as the anolyte.

Electrochemical Measurements

Chronoamperometry measurements were carried out in a custom-made PEEK flow cell setup similar to the one reported by Ager et al. (3) using a silver foil as the working electrode and a platinum foil as the counter electrode. The cathode compartment was separated from the anode compartment by a Selemion AMV anion-exchange membrane (AGC Engineering Co.). All potentials were measured versus a leakless Ag/AgCl reference electrode (Innovative Instruments) with an outer diameter of 5 mm that was inserted into the cathode compartment. The reference electrode was calibrated against ferrocenecarboxylicacid in a 0.2 M phosphate buffer solution at pH 7.0 (+0.239 V vs. Ag/AgCl). All electrochemical measurements were carried out using a Biologic VMP3 multichannel potentiostat.

Potentiostatic electrochemical impedance spectroscopy (PEIS) measurements were carried out prior to each electrolysis experiment to determine the Ohmic resistance of the flow cell. The impedance measurements were carried out at frequencies ranging from 200 kHz to 100 MHz to measure the solution resistance. A Nyquist plot was plotted and in the high-frequency part a linear fit was performed and the axis intersection was calculated. The value of this intersection represents the Ohmic resistance of the cell. An average of 3 measurements was taken to calculate the value of R. Typically, small resistances were measured, ranging from 40 to 60 Ω.

All chronoamperometric experiments were performed for 65 min at 25 °C using CO_2-saturated 0.1 M $KHCO_3$ as electrolyte. The potentiostat was set to compensate for 85 % of the Ohmic drop, with the remaining 15 % being compensated for after the measurements. The effluent gas stream coming from the flow cell (5 mL/min) was flowed into the sample loops of a gas chromatograph (GC-FID/TCD, SRI 8610C, in Multi Gas 5 configuration) equipped with HayeSep D and Molsieve 5A columns. Methane, and carbon monoxide were detected by a

methanizer-flame ionization detector (FID) and the hydrogen was detected by a thermal conductivity detector (TCD). Every 15 minutes, 2 mL of gas was sampled to determine the concentration of gaseous products. After electrolysis, the liquid products in both catholytes and anolytes were quantified by both HPLC (Thermo Scientific Ultimate 3000) and ^{1}H NMR. For ^{1}H NMR, solutions containing 90% electrolyte and 10% D_2O (v/v) with internal standard (N,N-dimethylformamide or dimethylsulfoxide) were prepared and measured using a water suppression technique on a Bruker 400 MHz NMR spectrometer.

All potentials were converted from the Ag/AgCl scale to the reversible hydrogen electrode (RHE) scale by using $V_{RHE} = V_{(Ag/AgCl)measured} - 0.197 - 0.059 \times pH$, where V_{RHE}, $V_{(Ag/AgCl)measured}$ and pH are potential vs RHE, measured potential vs Ag/AgCl reference electrode and pH of the electrolyte (6.8).

Linear sweep voltammetry (LSV) and cyclic voltammetry (CV) measurements were recorded at 25 ^oC using a two compartment H-cell, separated with a Selemion-AMV anion-exchange membrane, with a Ag disk working electrodes (diameter 3 mm), Pt counter electrode, and a Ag/AgCl reference electrode. The electrolyte solutions were either CO_2 or N_2 saturated 0.1 M $KHCO_3$ and contained 10 mM of additive when needed.

Rotation disk electrode experiments were done in a two compartments H-cell using a Ag disc electrode, a Pt foil as a counter electrode and a Ag/AgCl reference electrode using N_2-saturated $KHCO_3$ electrolyte with 10 mM of additive. The cathodic chamber was separated from the anodic chamber with an Selemion AMV anion-exchange membrane. The film was generated first without rotation for 15 min at –1.1 V. Chronoamperometry experiments were performed at different rotating rate (500 rpm, 1000 rpm, 2000 rpm, 3000 rpm and 5000 rpm) for 15 min at –1.1 V. The average current density over 15 min was used to generate the plot of the dependence of the rotation rate of the Ag electrode on the HER activity.

The order in $[HCO_3^-]$ was determined by performing chronoamperometry experiments in the same flow cell setup as previously described. Bulk electrolysis were done at –0.9 V vs. NHE, at different concentration of $KHCO_3$ varying from 0.1 M to 1 M, with or without 10 mM of **1-Br$_2$** or **2-Cl** dissolved in the electrolyte. As the pH (6.8 at 0.1 M and 7.6 at 1 M) and $[K^+]$ were also affected, control experiments were performed. Similar results were obtained by the addition of $HClO_4$ and/or KCl to the electrolyte to maintain the same pH and $[K^+]$, respectively, across the entire range of $[HCO_3^-]$ studied. Similar results were also obtained at –0.9 V vs RHE.

The CO_2 partial pressure dependence experiments were performed in the same flow cell set-up as previously described. Chronoamperometry experiments were performed at –0.9 V vs. NHE, at different partial pressure of CO_2 varying from 1 SCCM to 5 SCCM. N_2 was used as the balance gas to keep a total gas flow at 5 SCCM. As the pH was also affected, control experiments were performed. The trend in the partial current density of CO remained unaffected by performing the reactions at –0.9 V vs RHE or by using $HClO_4$ to keep the pH constant.

Electrochemical Active Surface Area (ECSA) and Partial Current Density Experiments
All experiments were done in the same flow cell as previously described for bulk electrolysis experiments. All HER experiments were done in N_2-saturated and all CO_2RR experiments were done in CO_2-saturated 0.1 M $KHCO_3$ electrolyte. We have intentionally investigated HER and CO_2RR separately to decouple the mass transfer properties of proton carriers and CO_2, and thus, to study the intrinsic effect of the molecular film on HER and CO_2RR. The ECSA was determined by CV by scanning a non-Faradaic region from –0.1 V to –0.2 V at different scan

rate (from 10 mV/s to 250 mV/s). The anodic and cathodic current values at –0.15 V were extracted. The plot of $j_{cathodic}$ and j_{anodic} against the scan rate were generated and gave straight lines. The slope of the curves was used as an estimate of the number of ECSA area. The current densities of H_2 were determined by bulk electrocatalysis either at –0.9 V or –1.1 V for 15 min. CO partial current densities were determined by performing bulk electrocatalysis at –0.9 V or –1.1 V for 35 min. The gas mixture was analyzed by in-line GC, using the same method as previously described for bulk electrocatalysis experiments. ECSA area and bulk electrolysis were always performed in a fresh, additive-free, 0.1 M $KHCO_3$ electrolyte.

The following protocol was rigorously followed for each experiments to ensure data reproducibility. The ECSA area and current densities for H_2 (for HER experiments) or for CO (for CO_2RR experiments) were first measured and determined on a freshly polished silver electrode. The cathodic electrolyte was then changed to a fresh electrolyte containing 10 mM of **2-Cl**. The film was generated by bulk electrolysis at –0.7 V for different times (from 10 ms to 1 h). The cathodic electrolyte was changed for a fresh electrolyte containing no additive. The ECSA area and bulk electrolysis were recorded again. The obtained data were normalized against each blank silver previously measured.

X-ray photoelectron spectroscopy (XPS)

X-ray photoelectron spectroscopy (XPS) data were collected using a Surface Science Instruments M-Probe ESCA controlled by Hawk Data Collection software (Service Physics, Bend OR; V7.04.04). The monochromatic X-ray source was the Al Kα line at 1486.6 eV, directed at 35° to the sample surface (55° off normal). Emitted photoelectrons were collected at an angle of 35° with respect to the sample surface (55° off normal) by a hemispherical analyzer. The angle between the electron collection lens and X-ray source is 71°. Low-resolution survey spectra were acquired between binding energies of 1-1000 eV. Higher-resolution detailed scans, with a resolution of ~0.8 eV, were collected on individual XPS lines of interest. The sample chamber was maintained at $< 2 \times 10^{-9}$ Torr. The XPS data were analyzed using the CasaXPS software. Post-catalysis silver foils were rinsed with copious amount of water, dried under a stream of nitrogen and immediately transferred to a nitrogen glove box before XPS measurements.

Atomic Force Microscopy (AFM)

All AFM images were recorded on a Bruker Dimension Icon using the ScanAssyst mode. A scanassyst-air canteliver was used with a spring constant of 0.4 N/m and a resonant frequency of 70 KHz.

Scanning Electron Microscopy (SEM) and Energy Dispersive Spectrometer (EDS)

All SEM images were recorded on a ZEISS 1550VP FESEM instrument, equipped with in-lens SE, below-lens SE, variable pressure SE and Robinson-type BSE detectors. EDS measurements were done on an Oxford X-Max SDD X-ray EDS system.

Physical vapor deposited (PVD) silver electrode preparation

PVD electrode were used to perform cross sectional SEM imaging of the film. These electrodes can cleanly be cut without disrupting the film deposited on the surface of the electrode.

Supporting Figures and Tables

Table S1. Faradaic efficiency (%) for CO_2RR products and hydrogen obtained during CO_2RR on bare silver in a CO_2 saturated 0.1 M $KHCO_3$ electrolyte at different applied potential.

Potential (V)	Run	Faradaic Efficiency (%)					j (mA/cm^2)
		H_2	CO	HCOOH	CH_4	Total	
–0.60	1	91.0	2.4	0.0	0.0	93.4	–0.13
	2	82.1	2.1	0.0	0.0	84.2	–0.14
	Average	86.5	2.3	0.0	0.0	88.8	–0.14
–0.70	1	89.1	5.2	0.0	0.0	94.3	–0.30
	2	87.2	5.1	0.0	0.0	92.3	–0.32
	Average	88.2	5.1	0.0	0.0	93.3	–0.31
–0.79	1	89.6	4.5	0.0	0.0	94.1	–0.71
	2	84.3	9.0	0.0	0.0	93.3	–0.48
	Average	86.9	6.7	0.0	0.0	93.7	–0.60
–0.89	1	65.0	23.7	5.0	0.0	93.7	–0.97
	2	56.9	36.2	5.8	0.0	98.8	–0.79
	Average	60.91	30.0	5.4	0.0	96.3	–0.88
–0.99	1	29.8	64.4	4.4	0.0	98.6	–1.46
	2	30.7	60.1	4.2	0.0	95.0	–1.44
	Average	30.2	62.2	4.3	0.0	96.8	–1.45
–1.09	1	22.4	68.1	3.4	0.0	93.9	–2.64
	2	17.3	77.4	3.4	0.0	98.1	–2.47
	3	16.0	77.8	3.4	0.0	97.2	–3.14
	Average	18.6	74.4	3.4	0.0	96.4	–2.75
–1.16	1	21.3	57.5	4.4	0.0	83.2	–4.31
	2	29.6	62.0	4.7	0.0	96.3	–4.81
	Average	25.5	59.7	4.6	0.0	89.7	–4.56
–1.23	1	44.4	44.4	4.6	0.1	93.4	–7.94
	2	54.6	32.2	3.2	0.1	90.1	–8.43
	Average	49.5	38.3	3.9	0.1	91.7	–8.19
–1.30	1	72.1	14.5	1.9	0.1	88.6	–11.91
	2	79.4	11.2	1.2	0.2	91.9	–15.60
	Average	75.7	12.9	1.6	0.2	90.3	–13.76

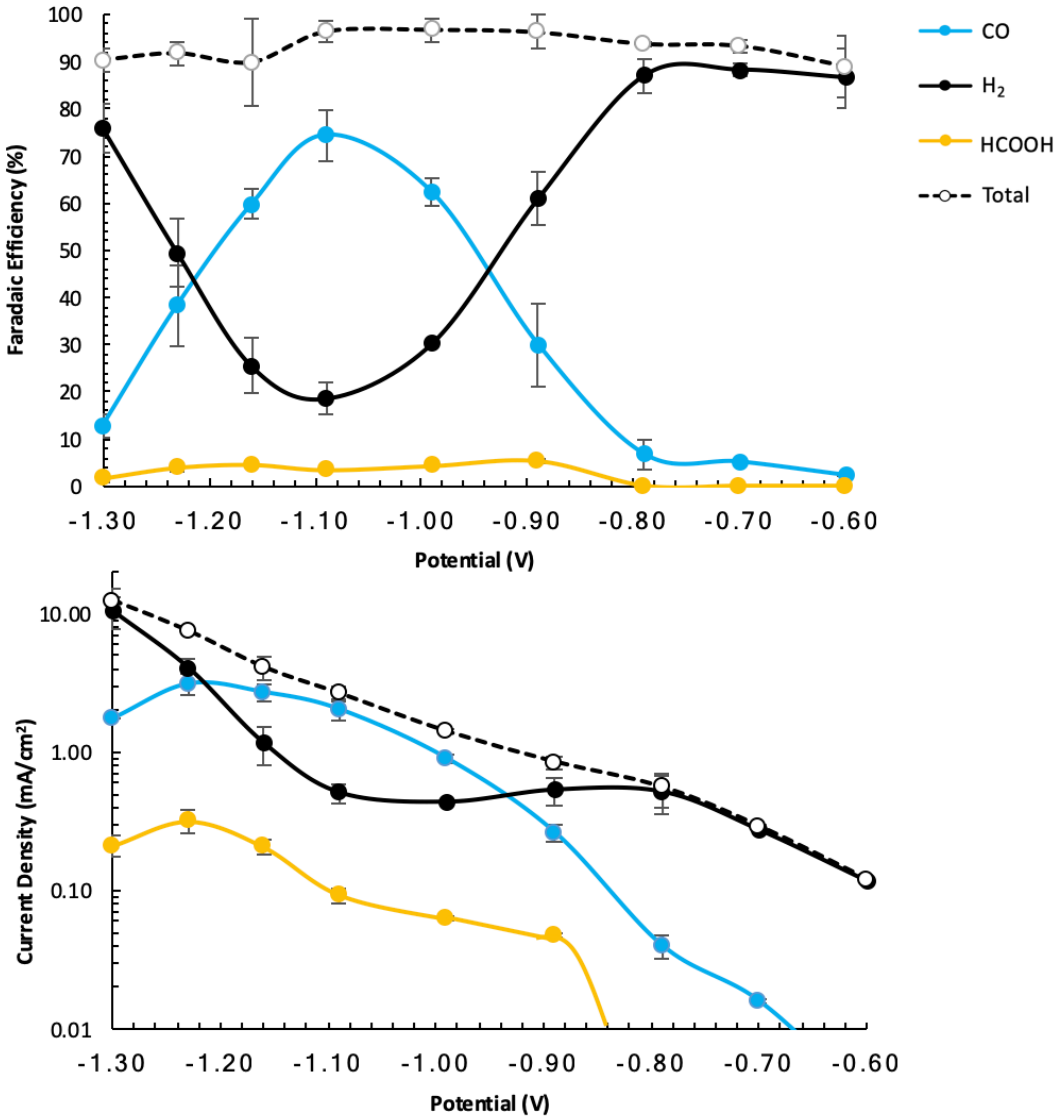

Fig. S1. (a) Faradaic efficiencies and (b) partial current densities for CO_2RR products and hydrogen as a function of potential during CO_2RR in a CO_2-saturated 0.1 M $KHCO_3$ electrolyte on bare silver.

Table S2. Faradaic efficiency (%) for CO_2RR products and hydrogen obtained during CO_2RR on silver in CO_2 saturated 0.1 M $KHCO_3$ electrolyte in the presence of 10 mM **1-Br$_2$** at different applied potential.

Potential (V)	Run	Faradaic Efficiency (%)					j (mA/cm^2)
		H_2	CO	HCOOH	CH_4	Total	
–0.75	1	*N.D	4.3	0.0	0.0	4.3	–0.10
	2	N.D	7.2	0.0	0.0	7.2	–0.05
	Average	N.D	5.7	0.0	0.0	5.7	–0.08
–0.79	1	79.2	5.1	0.0	0.0	84.3	–0.16
	2	73.0	5.8	0.0	0.0	78.8	–0.17
	Average	76.1	5.4	0.0	0.0	81.5	–0.17
–0.85	1	41.3	49.7	0.0	0.0	91.0	–0.29
	2	40.1	57.1	0.0	0.0	97.2	–0.15
	Average	40.7	53.4	0.0	0.0	94.1	–0.22
–0.89	1	7.3	82.2	9.8	0.0	99.3	–0.28
	2	16.7	77.8	6.0	0.0	100.5	–0.25
	Average	12.0	80.0	7.9	0.0	99.9	–0.27
–0.99	1	0.0	102.0	0.0	0.0	102.0	–1.05
	2	0.0	97.2	0.0	0.0	97.2	–1.13
	Average	0.0	99.6	0.0	0.0	99.6	–1.09
–1.09	1	0.0	94.0	3.4	0.0	97.4	–1.66
	2	1.3	92.3	8.6	0.0	102.1	–1.96
	3	0.9	92.0	3.4	0.0	96.2	–1.73
	Average	0.7	92.7	5.1	0.0	98.6	–1.78
–1.16	1	23.1	67.6	8.6	0.0	99.3	–1.57
	2	19.7	64.8	9.3	0.0	93.8	–1.51
	Average	21.4	66.2	8.9	0.0	96.6	–1.54
–1.23	1	32.0	49.1	9.9	0.0	91.1	–2.48
	2	33.5	48.3	10.4	0.0	92.2	–2.45
	Average	32.8	48.7	10.2	0.0	91.2	–2.47
–1.30	1	81.4	7.1	1.7	0.0	90.3	–8.49
	2	81.4	7.1	1.9	0.0	90.5	–8.26
	Average	81.4	7.1	1.8	0.0	90.3	–8.38

*N.D: non detectable

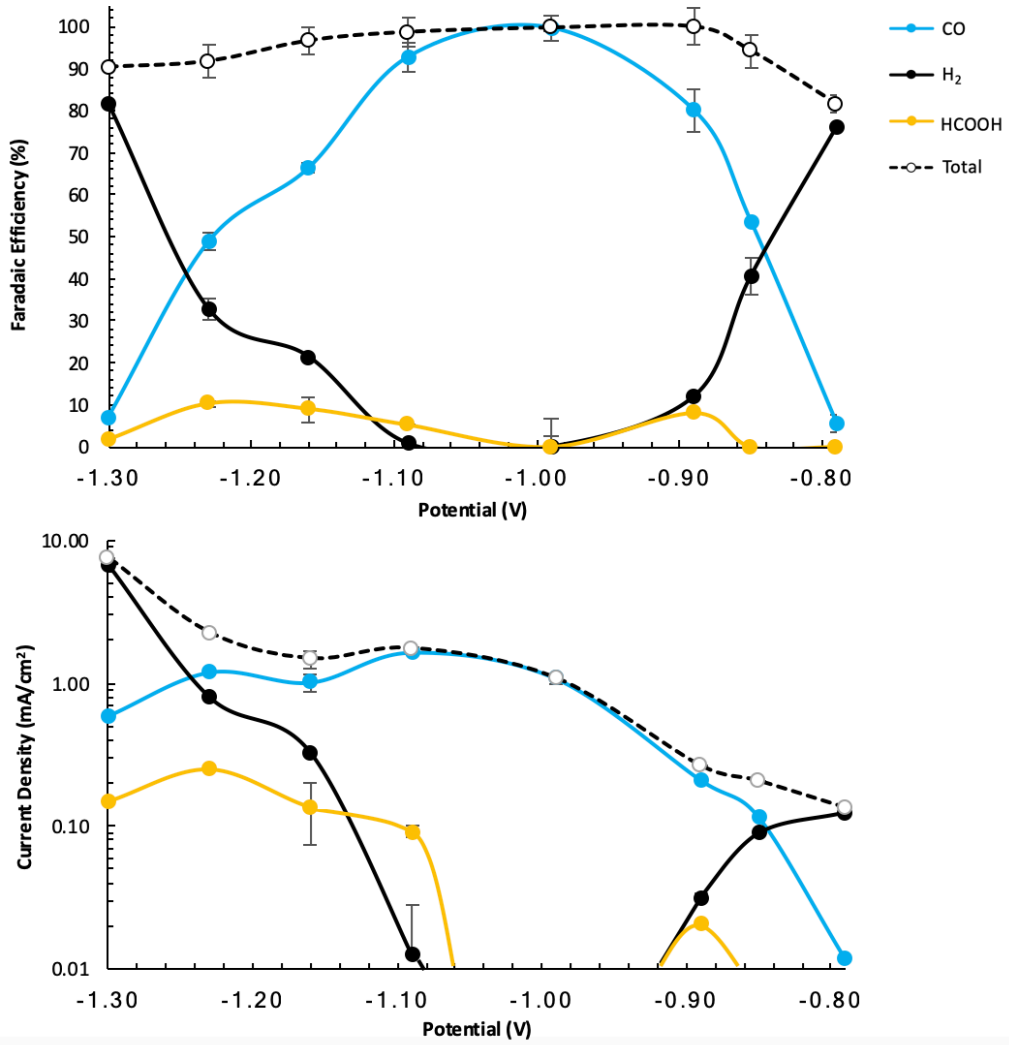

Fig. S2. (a) Faradaic efficiencies and (b) partial current densities for CO_2RR products and hydrogen as a function of potential during CO_2RR in a CO_2-saturated 0.1 M $KHCO_3$ electrolyte in the presence of 10 mM **1-Br$_2$**.

Table S3. Faradaic efficiency (%) for CO_2RR products and hydrogen obtained during CO_2RR on silver in CO_2 saturated 0.1 M $KHCO_3$ electrolyte in the presence of 10 mM **2-Cl** at different applied potential.

Potential (V)	Run	Faradaic Efficiency (%)					j (mA/cm^2)
		H_2	CO	HCOOH	CH_4	Total	
–0.80	1.00	N.D*	21.6	0.0	0.0	21.6	–0.02
	2.00	N.D	18.5	0.0	0.0	18.5	–0.03
	Average	0.0	20.0	0.0	0.0	20.0	–0.02
–0.85	1	N.D	31.4	0.0	0.0	31.4	–0.03
	2	N.D	16.0	0.0	0.0	16.0	–0.03
	Average	0.0	23.7	0.0	0.0	23.7	–0.03
–0.89	1	N.D	31.7	0.0	0.0	31.7	–0.04
	2	N.D	35.2	0.0	0.0	35.2	–0.04
	Average	0.0	33.4	0.0	0.0	33.4	–0.04
–0.99	1	0.0	95.2	0.0	0.0	95.2	–0.23
	2	0.0	93.5	0.0	0.0	93.5	–0.20
	Average	0.0	94.4	0.0	0.0	94.4	–0.22
–1.09	1	0.0	90.5	0.0	0.0	90.5	–0.88
	2	0.0	95.7	0.0	0.0	95.7	–0.81
	Average	0.0	93.6	0.0	0.0	93.6	–0.85
–1.16	1	12.4	55.5	5.2	0.0	73.1	–2.97
	2	11.1	60.1	5.4	0.0	76.7	–3.69
	Average	11.8	57.8	5.3	0.0	74.9	–3.33
–1.23	1	41.0	31.4	5.1	0.0	77.6	–5.51
	2	42.0	30.3	4.6	0.0	76.9	–6.33
	Average	41.5	30.9	4.9	0.0	77.3	–5.92
–1.30	1	65.4	13.7	2.2	0.0	81.3	–11.41
	2	64.6	13.7	3.0	0.0	81.4	–7.98
	Average	65.0	13.7	2.6	0.0	81.4	–9.70

*N.D: non detectable

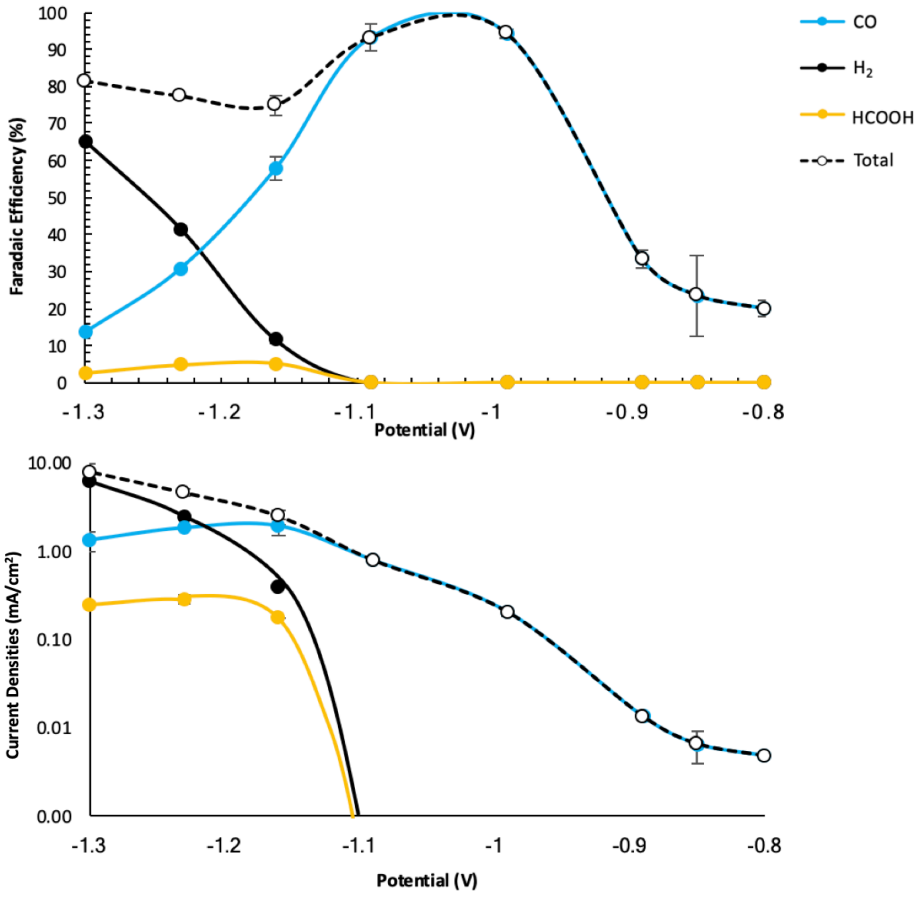

Fig. S3. (a) Faradaic efficiencies and (b) partial current densities for CO_2RR products and hydrogen as a function of potential during CO_2RR in a CO_2-saturated 0.1 M $KHCO_3$ electrolyte in the presence of 10 mM **2-Cl**.

Table S4. Faradaic efficiency (%) for CO_2RR products and hydrogen obtained during a catalytic run in a CO_2-saturated 0.1 M $KHCO_3$ electrolyte at –0.99 V with **1-Br$_2$** (run 1); without additive in the electrolyte and using the resulting electrode from run 1 (run 2).

Additive	Run	Faradaic Efficiency (%)					j (mA/cm^2)
		H_2	CO	HCOOH	CH_4	Total	
1-Br$_2$	1	0.0	99.5	0.0	0.0	99.5	–1.12
-	2	0.0	101.3	0.0	0.0	101.3	–1.03
2-Cl	1	0.0	92.5	0.0	0.0	92.5	–0.21
-	2	0.0	94.2	0.0	0.0	94.2	–0.24

Table S5. Faradaic efficiency (%) for CO_2RR products and hydrogen obtained during CO_2RR on silver in CO_2 saturated phosphate buffer, at different pH, at –1.1 V, in the presence of 10 mM of **1-Br$_2$**.

pH	Run	Faradaic Efficiency (%)					j (mA/cm^2)
		H_2	CO	HCOOH	CH_4	Total	
4.2	1	0.0	91.1	7.0	0.0	98.1	–1.8
4.2	2	0.0	92.3	6.9	0.0	99.2	–1.6
4.2	Average	0.0	91.7	7.0	0.0	98.7	–1.7
5.2	1	0.0	88.9	7.6	0.0	96.5	–2.0
5.2	2	0.0	87.3	9.7	0.0	97.0	–2.2
5.2	Average	0.0	88.1	8.6	0.0	96.7	–2.1
5.9	1	0.0	92.4	8.2	0.0	92.4	–1.7
5.9	2	0.0	91.2	19.3	0.0	91.3	–1.7
5.9	Average	0.0	91.2	8.7	0.0	91.2	–1.7
6.2	1	0.0	91.8	9.0	0.0	100.7	–1.7
6.2	2	0.0	92.5	9.1	0.0	101.5	–1.8
6.2	Average	0.0	92.1	9.0	0.0	101.1	–1.7
6.5	1	0.0	82.1	11.2	0.0	93.3	–2.4
6.5	2	0.0	90.1	9.6	0.0	99.6	–1.9
6.5	Average	0.0	86.1	10.4	0.0	96.5	–2.1

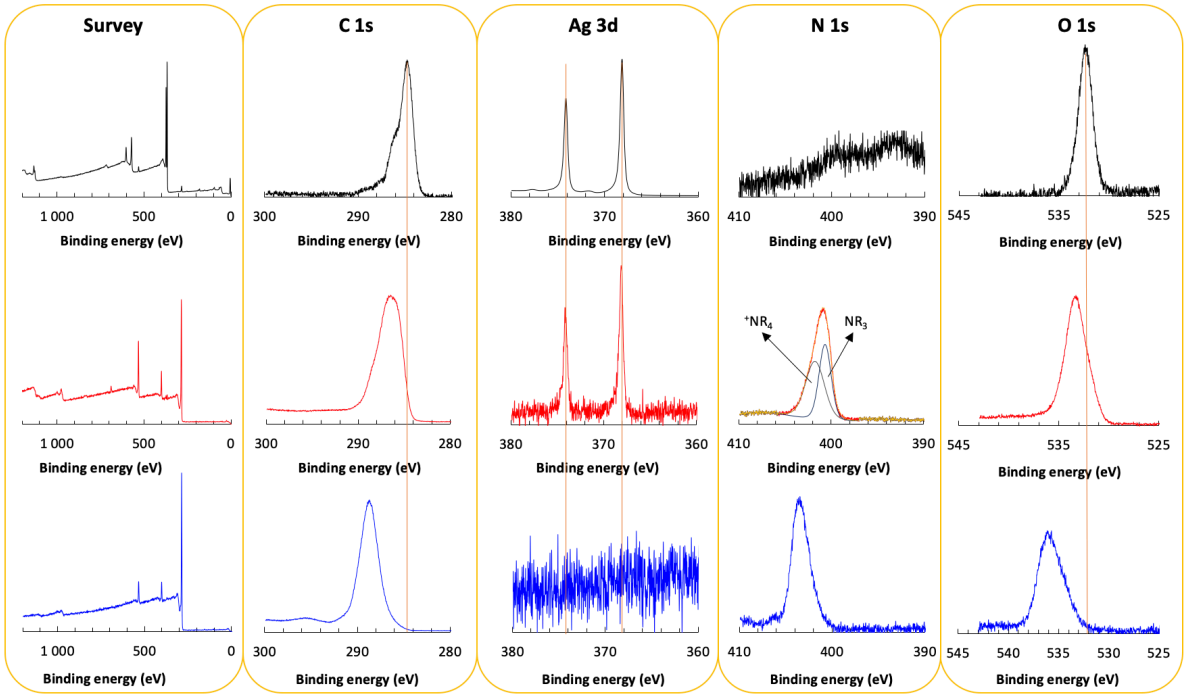

Fig. S4. Normalized X-ray photoelectron spectra after 65 min of electrolysis at –1.07 V in CO_2-saturated 0.1M $KHCO_3$ of (a) Ag; (b) **Ag-1**; (c) **Ag-2**.

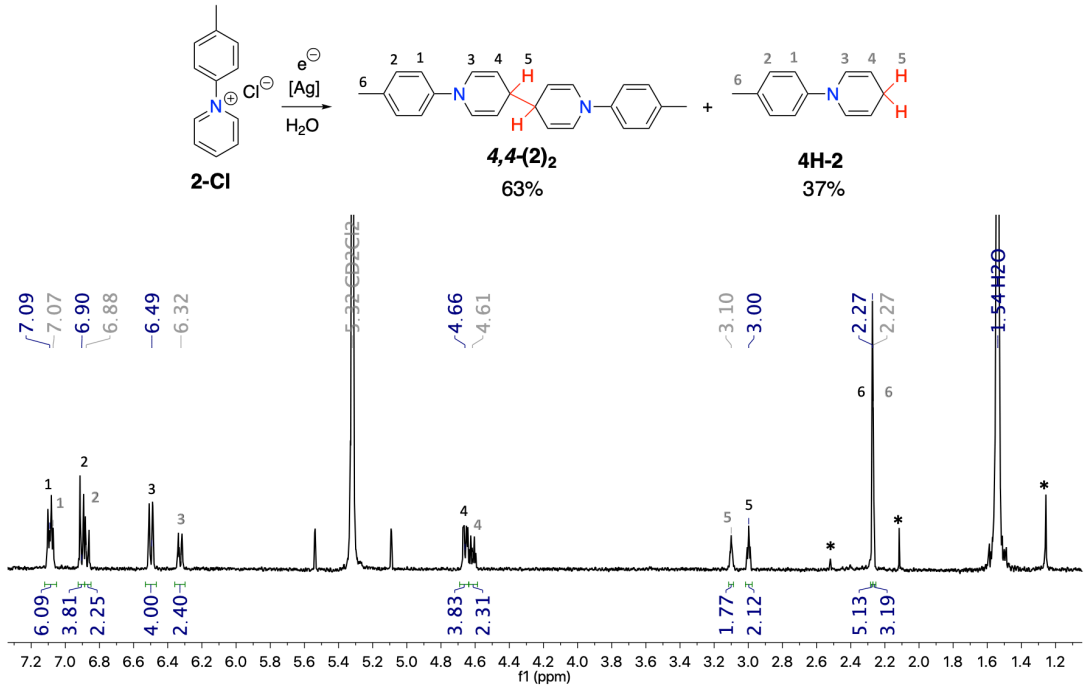

Fig. S5. Proposed structure of the different constituent of the film extracted from **Ag-2** (top), **4,4-(2)$_2$** and **4H-2**. ^{1}H NMR spectrum (bottom, CD_2Cl_2, 298 K) of the organic film extracted from a post catalysis Ag electrode at –1.1 V in a CO_2 saturated 0.1 M $KHCO_3$ electrolyte with 10 mM of **2-Cl**.

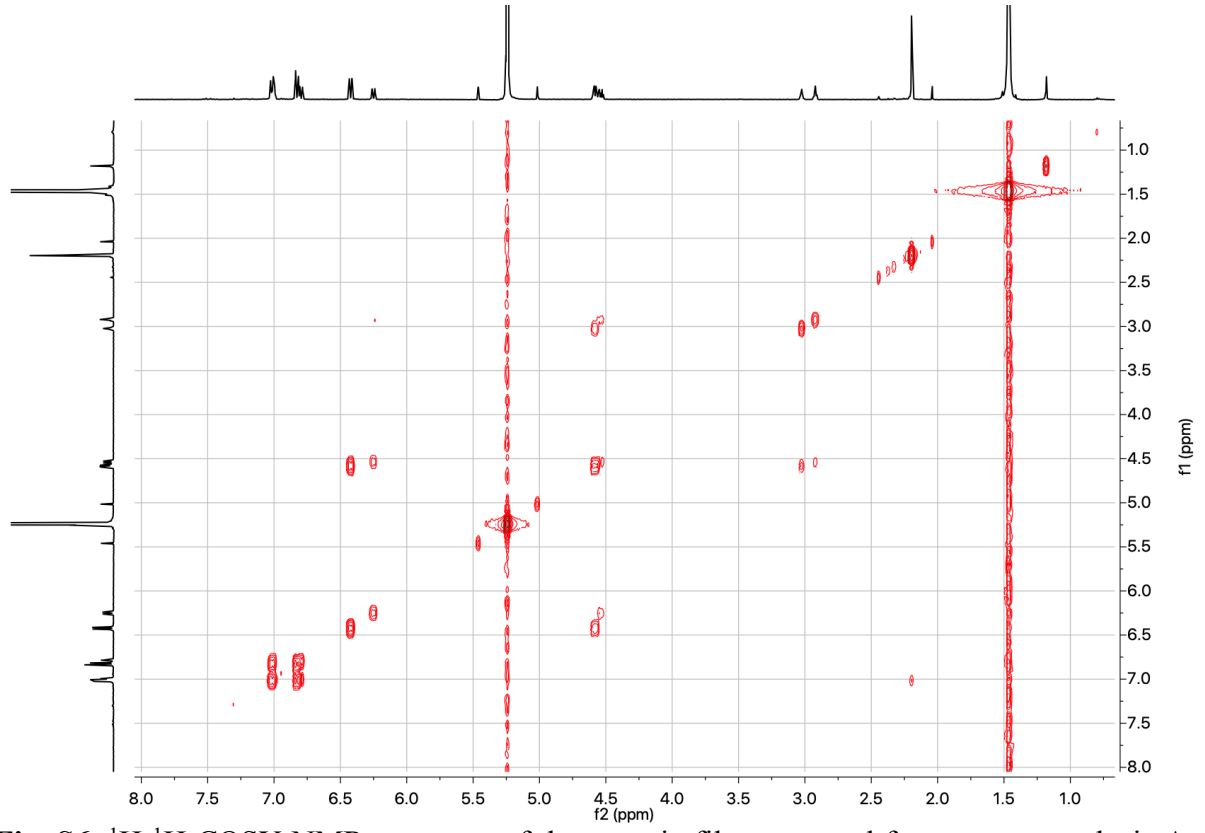

Fig. S6. ^{1}H-^{1}H COSY NMR spectrum of the organic film extracted from a post catalysis Ag electrode at –1.1 V in a CO_2-saturated 0.1 M $KHCO_3$ electrolyte with 10 mM of **2-Cl**. (CD_2Cl_2, 298 K).

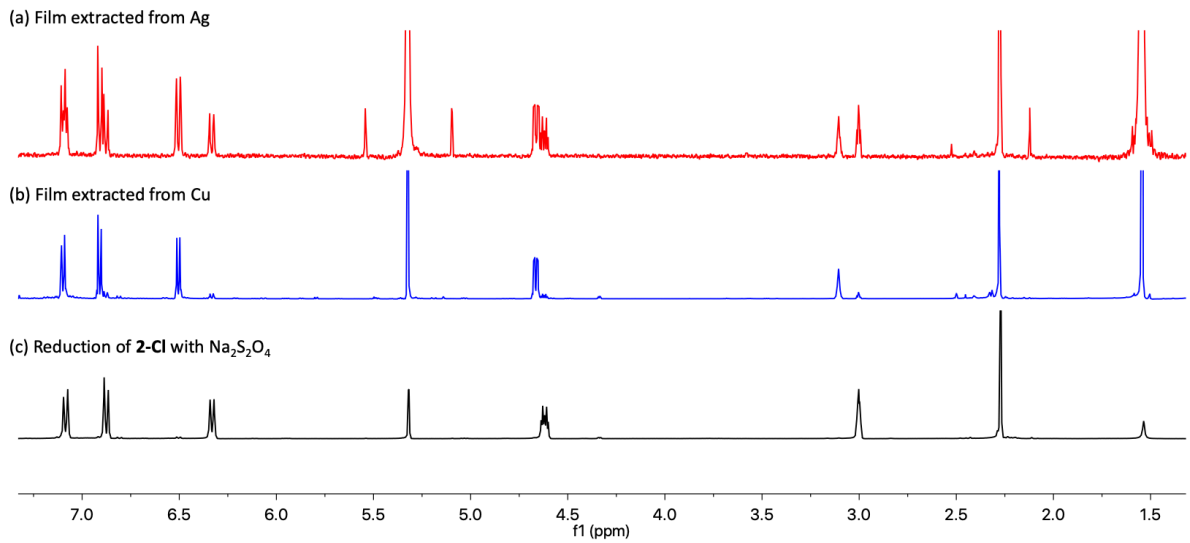

Fig. S7. Stack of ^{1}H NMR spectra (CD_2Cl_2, 298 K) of (a) the extracted film from **Ag-2**; (b) the extracted film from a postcatalysis Cu electrode at –1.1 V in a CO_2 saturated 0.1 M $KHCO_3$ electrolyte with 10 mM of **2-Cl**; (c) the reduction of **2-Cl** with $Na_2S_2O_4$ in basic water.

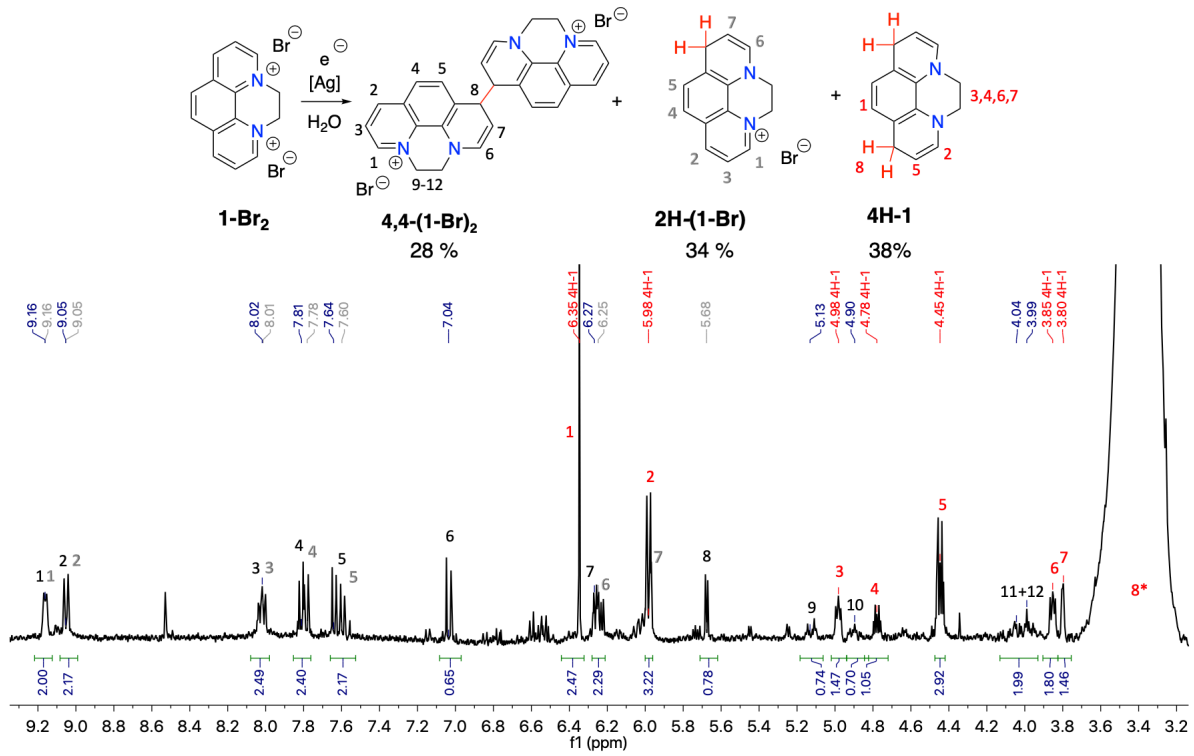

Fig. S8. Proposed structure of the different constituent of the film extracted from **Ag-1** (top), **4,4-(1-Br)$_2$**, **2H-(1-Br)** and **4H-1** (black, grey and red, respectively). ^{1}H NMR spectrum (bottom, DMSO-d_6, 298 K) of the organic film extracted from a post catalysis Ag electrode at –1.4 V in a CO_2 saturated 0.1 M $KHCO_3$ electrolyte with 10 mM of **1-Br$_2$**.

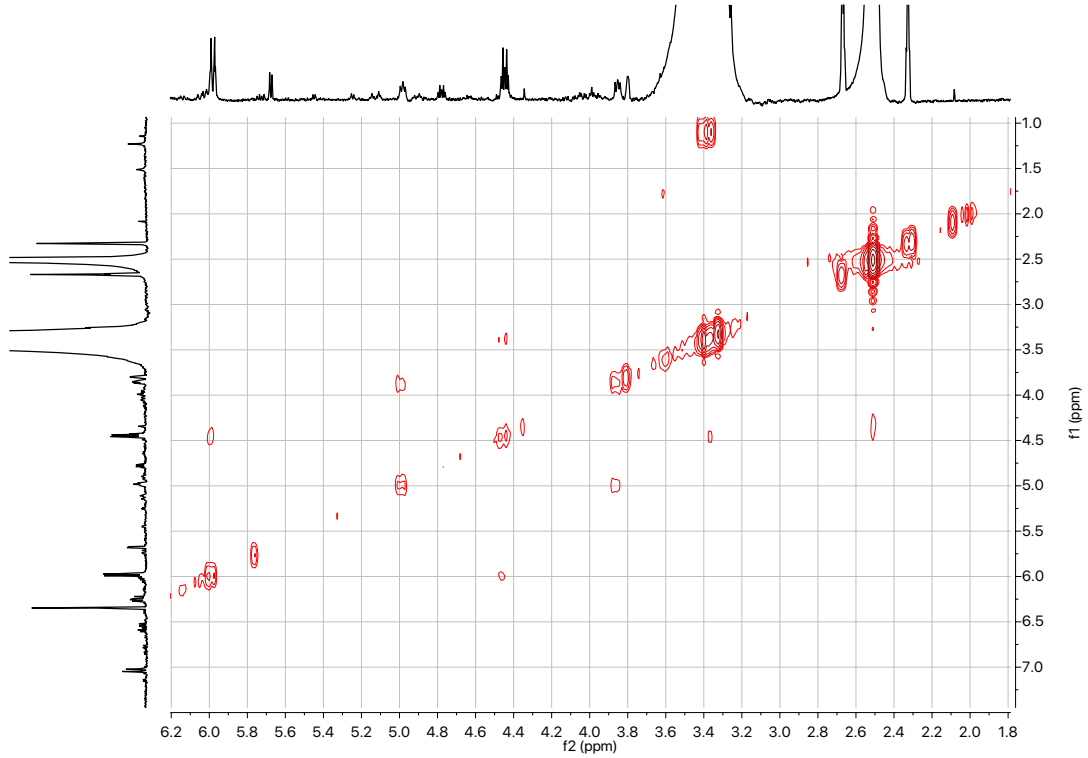

Fig. S9. ^{1}H-^{1}H COSY NMR spectrum of the organic film extracted from a post catalysis Ag electrode at –1.1 V in a CO_2-saturated 0.1 M $KHCO_3$ electrolyte with 10 mM of **1-Br$_2$**. (DMSO-d_6, 298 K).

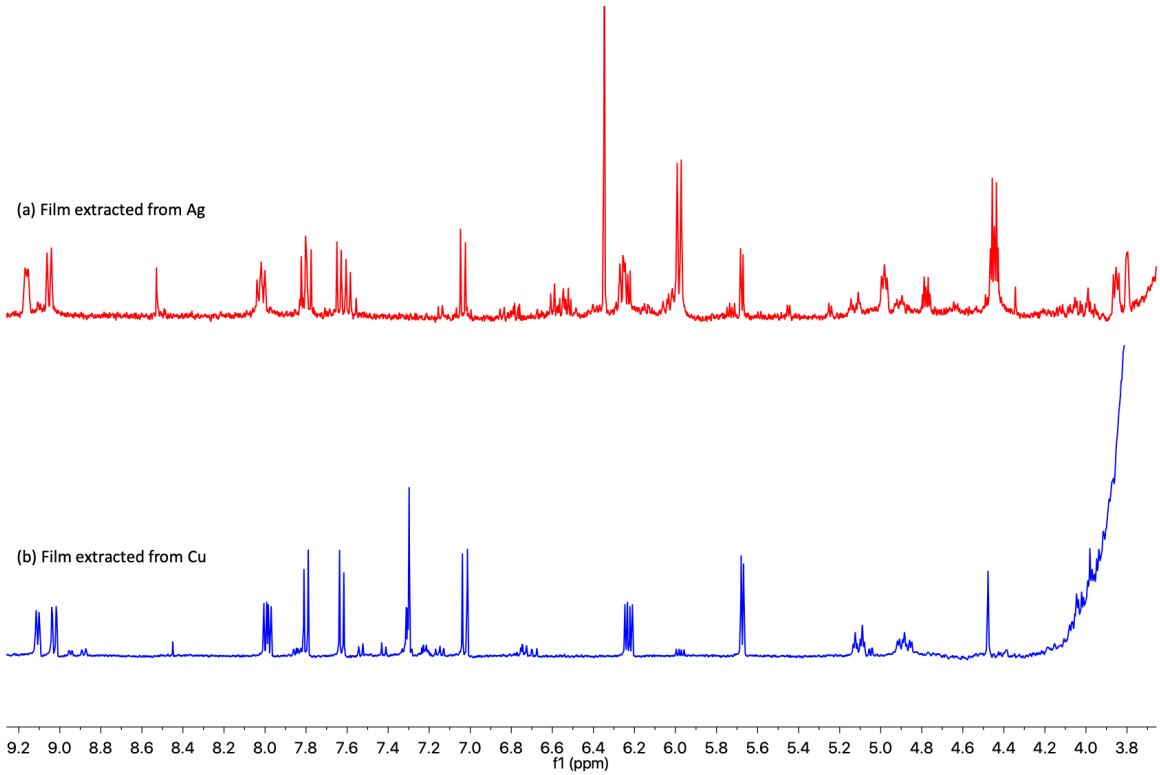

Fig. S10. Stack of ^{1}H NMR spectra (DMSO-d_6, 298 K) of (a) the extracted film from **Ag-1**; (b) the extracted film from a postcatalysis Cu electrode at –1.1 V in a CO_2 saturated 0.1 M $KHCO_3$ electrolyte with 10 mM of **1-Br$_2$**.

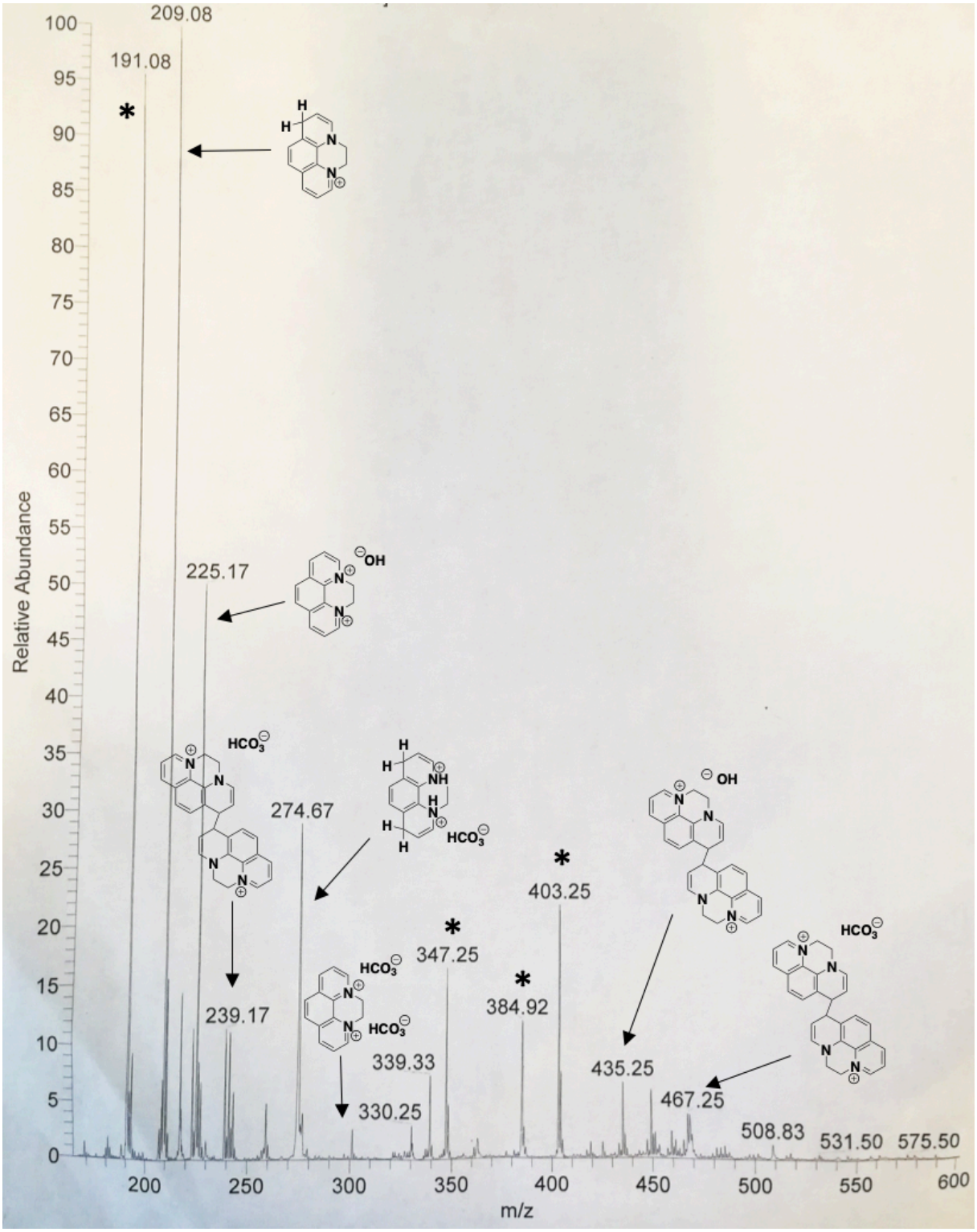

Fig. S11. ESI-MS spectrum of the film extracted from **Ag-1**. *Potential decomposition products.

Assignment of the film constituents in **Ag-1**:

4,4-(1-Br)$_2$: The stack of ^{1}H NMR spectra of the extracted film on Ag and Cu, depicted in Fig. S10, clearly shows that **Ag-1** contains ca. 28% of **4,4-(1-Br)$_2$**.

2H-(1-Br): In the ^{1}H NMR spectrum of **Ag-1** (Fig. S8), the integration of the two doublets at 9.16 ppm and 9.05 ppm, corresponding to the alpha protons of the pyridinium ring (labelled 1 and 2 in Fig. S8), are two times higher than expected. In addition, in Fig. S10, it can be seen that the resonances at 8.01 ppm, 7.81 ppm and 7.64 ppm, attributed to **4,4-(1-Br)$_2$**, are split into two signals in the spectrum of **Ag-1** compare to the ^{1}H NMR spectrum of the film extracted on copper. This suggests that there is another constituent of the film, structurally related to **4,4-(1-Br)$_2$**. Unfortunately, the signals of the ^{1}H-^{1}H COSY spectrum were too weak to further characterize this constituent of the film. Instead, the extracted film was analyzed by ESI-MS. The mass spectrum of the film shows an intense peak at 209.08 m/z. Based on the film composition of **Ag-2**, the ^{1}H NMR and the mass spectra of **Ag-1**, the second constituent of the film is tentatively associated to **2H-(1-Br)** ($M_{\mathbf{2H\text{-}(1\text{-}Br)}}^+$ = 209.11 g/mol). Based on integration, **2H-(1-Br)** represents ca. 34% of the film constituent.

4H-1: A last set of resonances is present in the ^{1}H NMR spectrum of **Ag-1**. The ^{1}H NMR and ^{1}H-^{1}H COSY spectra suggest the presence of a symmetric molecule with an aromatic:alkenyl protons ratio of 1:2. Based on the previous observation on **Ag-2** and the other constituents of the film of **Ag-1**, these resonances have been attributed to a doubly-reduced species **4H-1** (38%).

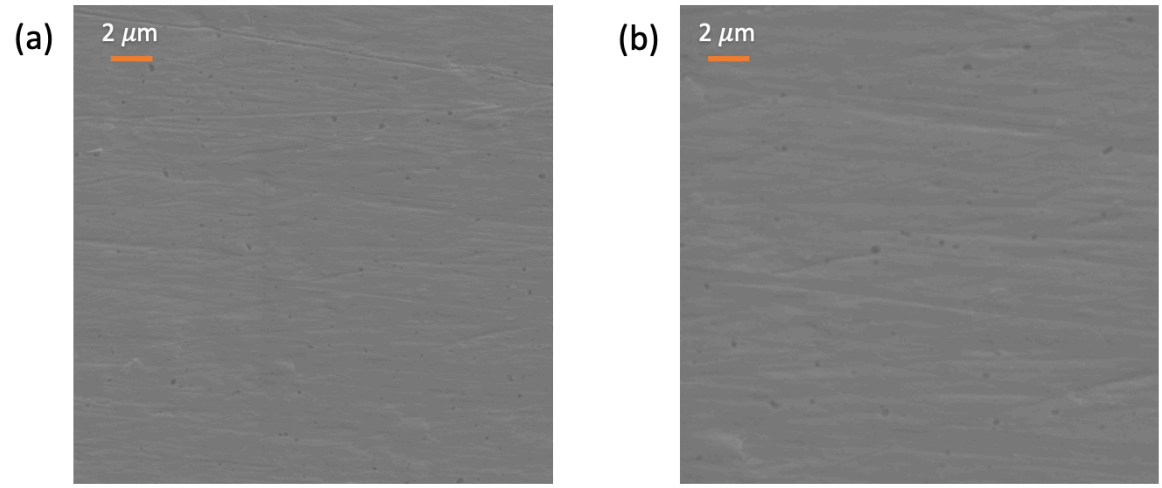

Fig. S12. *Ex-situ* SEM images of (a) a freshly polished Ag electrode (b) a post-catalysis Ag electrode after 65 min at –1.1 V in a CO_2 saturated 0.1 M $KHCO_3$ electrolyte without additive.

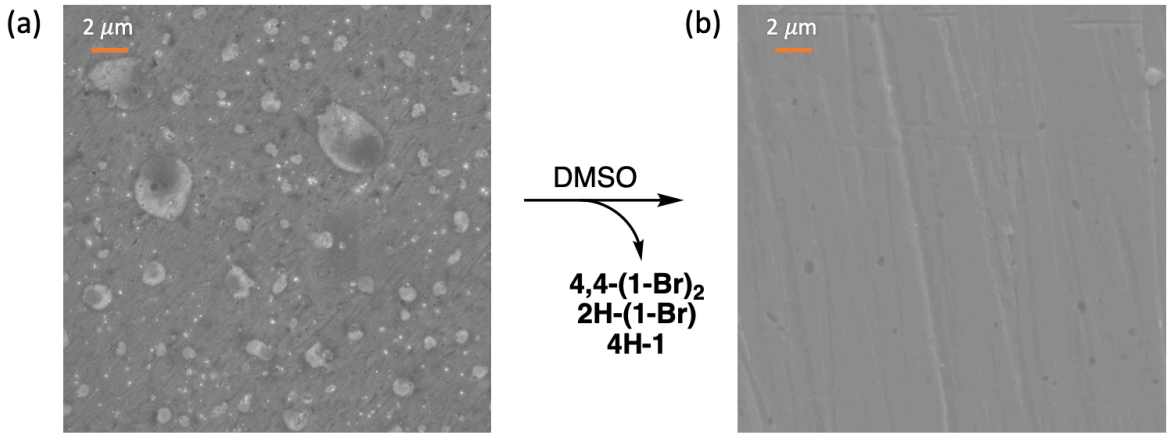

Fig. S13. *Ex-situ* SEM images of (a) **Ag-1**; (b) after extracting the organic film with DMSO-d_6.

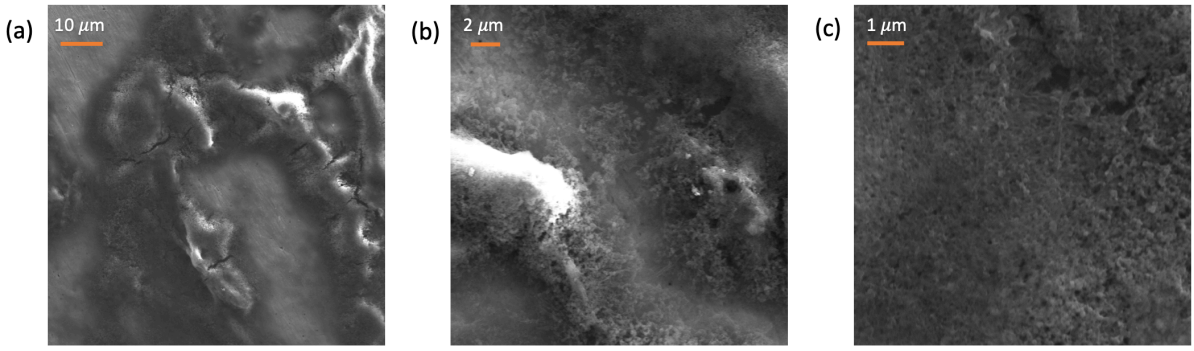

Fig. S14. *Ex situ* SEM images of **Ag-1** after 65 min of electrodeposition of a 10 mM **1-Br$_2$** dissolved in CO_2-saturated 0.1 M $KHCO_3$, at –1.4 V, at different magnification [(a) 3 kX; (b) 10 kX; (c) 45 kX]. These set of images further suggest that even when a thicker film is deposited on Ag, the electrode is only partially covered by a thick organic layer. The images also show that the thicker film is porous similarly to the film produced from **Ag-2**.

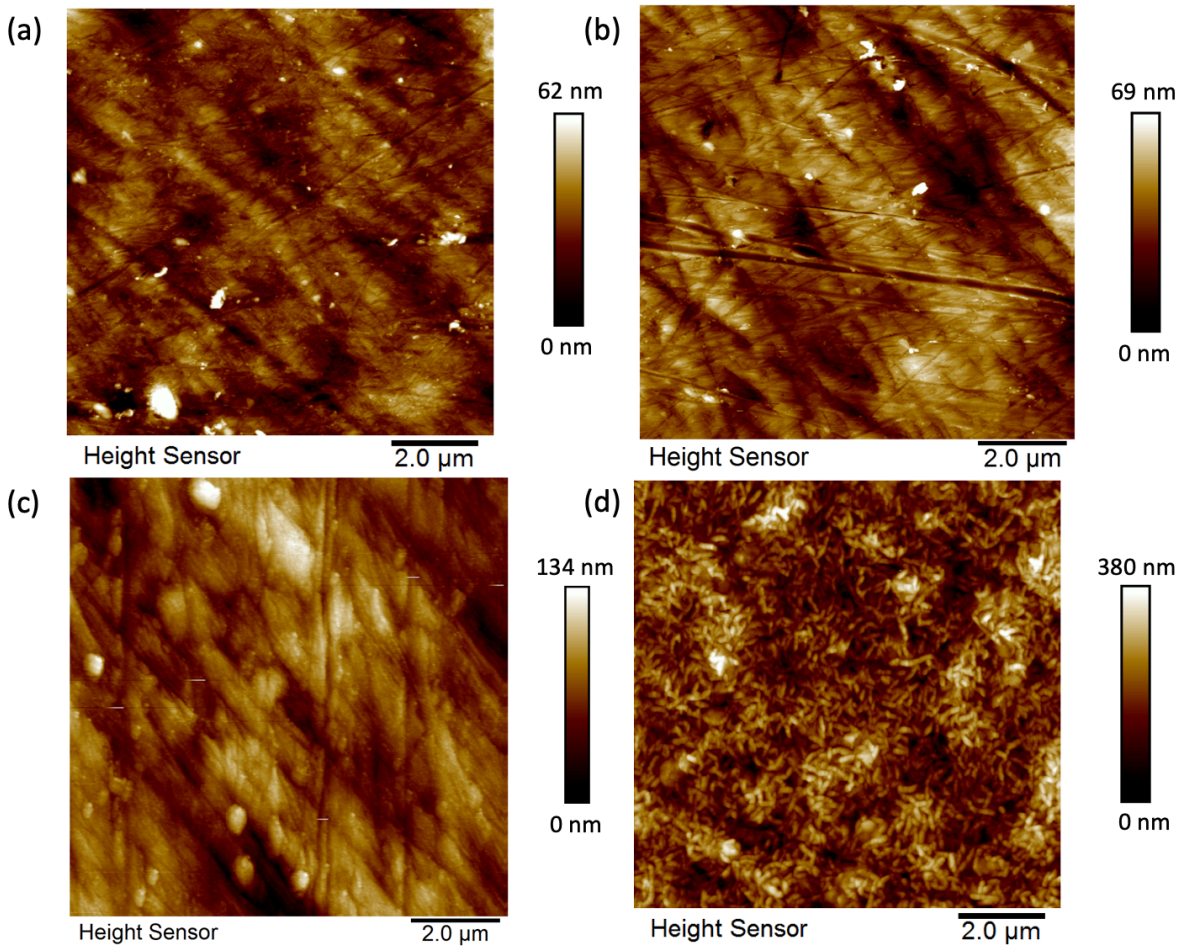

Fig. S15. *Ex-situ* AFM images of (a) a freshly polished Ag electrode; post-catalysis Ag electrode after 65 min of electrocatalysis at –1.1 V in a CO_2 saturated 0.1 M $KHCO_3$ electrolyte (b) without additive or with 10 mM of (c) **1-Br$_2$** or (d) **2-Cl**.

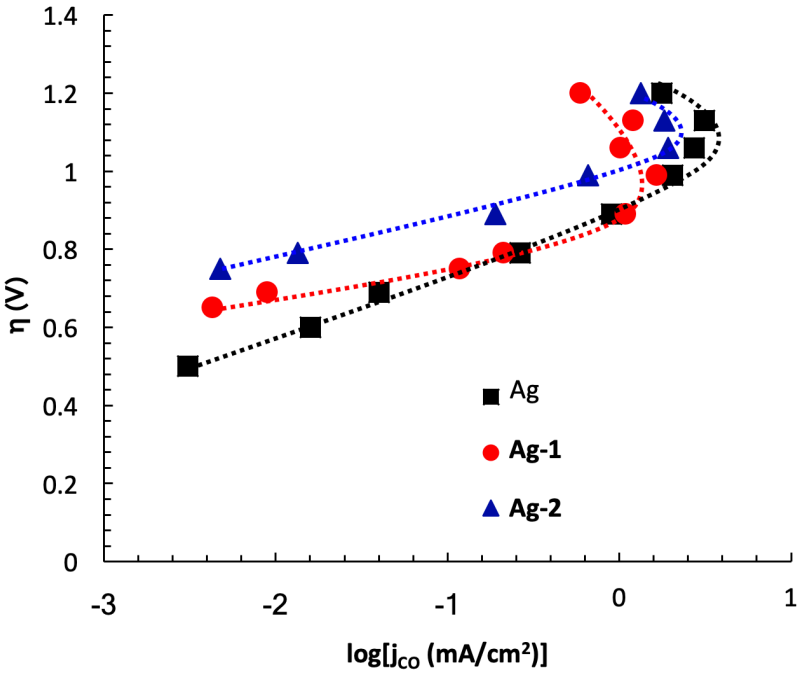

Fig. S16. Full Tafel plot recorded in CO_2-saturated 0.1 M $KHCO_3$ electrolyte for Ag (■), **Ag-1** (●) and **Ag-2** (▲). The lower CO rates observed at higher overpotential could arise from the depletion of the $*CO_2^{\bullet-}$ intermediate on the electrode due to the high CO_2RR and HER rates and CO_2 diffusion limitations to the electrode interface.(4) As can be seen, this behavior is observed for Ag, **Ag-1**, and **Ag-2**, suggesting that this CO_2 mass transport limitation and the depletion of the $*CO_2^{\bullet-}$ intermediate is an intrinsic problem of the silver electrode, and is not induced by the organic film.

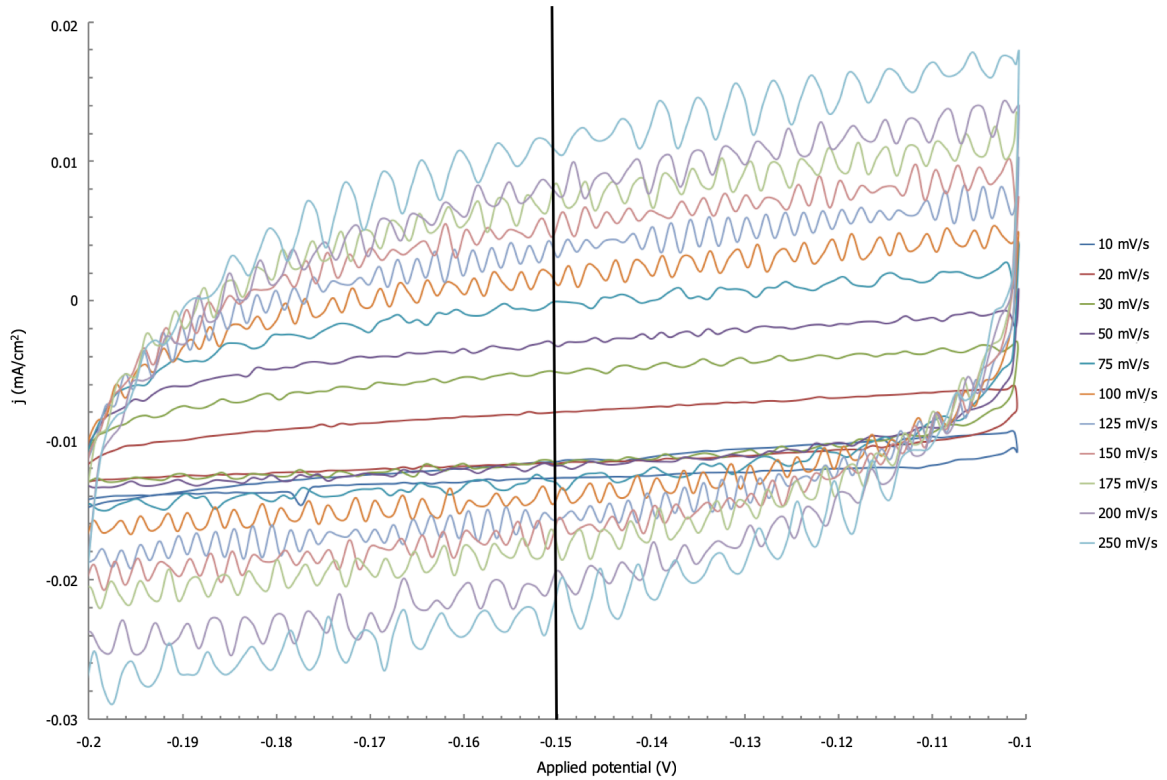

Fig. S17. Typical example of voltammograms obtained from scanning between –0.1 V to –0.2 V at different scan rate. The black line at –0.15 V represents the potential used to determine the ECSA of the silver electrode.

Table S6. Cathodic and anodic currents recorded by CV scans at different rates at –0.15 V in a CO_2 saturated 0.1 M $KHCO_3$ for bare Ag.

Scan rate (mV/s)	Cathodic current ($j_{cathodic}$, mA/cm^2)	Anodic current (j_{anodic}, mA/cm^2)
10	-7.97E-03	-5.90E-03
20	-8.34E-03	-4.17E-03
30	-9.77E-03	-2.70E-03
50	-1.06E-02	-1.22E-03
75	-1.18E-02	2.74E-04
100	-1.32E-02	3.02E-03
125	-1.67E-02	4.69E-03
150	-1.71E-02	4.99E-03
175	-1.84E-02	8.43E-03
200	-2.342270E-02	8.58E-03
250	-2.22E-02	9.97E-03

Table S7. Cathodic and anodic currents recorded by CV scans at different rates at –0.15 V in a CO_2 saturated 0.1 M $KHCO_3$ after 1 min of electrodeposition of **2-Cl**.

Scan rate (mV/s)	Cathodic current ($j_{cathodic}$, mA/cm^2)	Anodic current (j_{anodic}, mA/cm^2)
10	–5.18E–03	–3.80E–03
20	–6.01E–03	–2.57E–03
30	–6.39E–03	–1.74E–03
50	–7.52E–03	–8.20E–04
75	–8.93E–03	3.17E–04
100	–9.55E–03	1.01E–03
125	–1.12E–02	2.48E–03
150	–1.19E–02	2.55E–03
175	–1.32E–02	3.12E–03
200	–1.45E–02	4.89E–03
250	–1.58E–02	5.78E–03

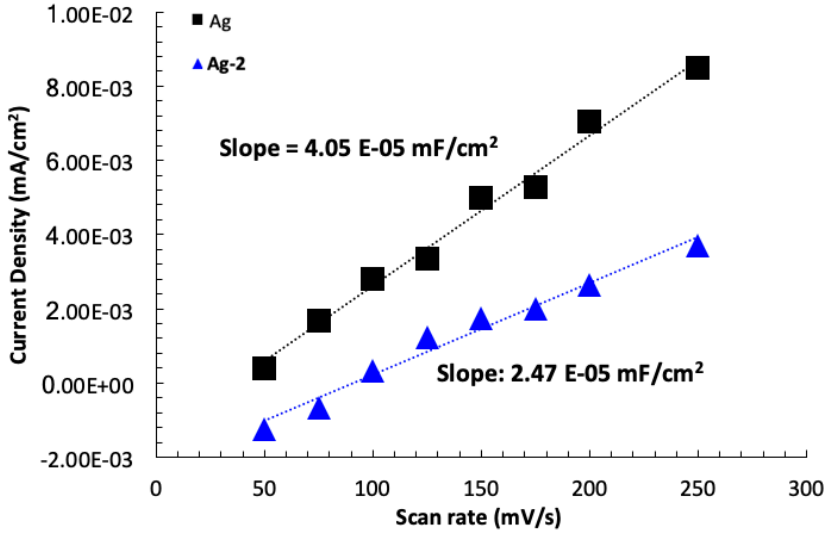

Fig. S18. Plot of the CV scan rates against the anodic current density for Ag (■) and **Ag-2** (▲). The slope of the linear curves was used to determine the ECSA.

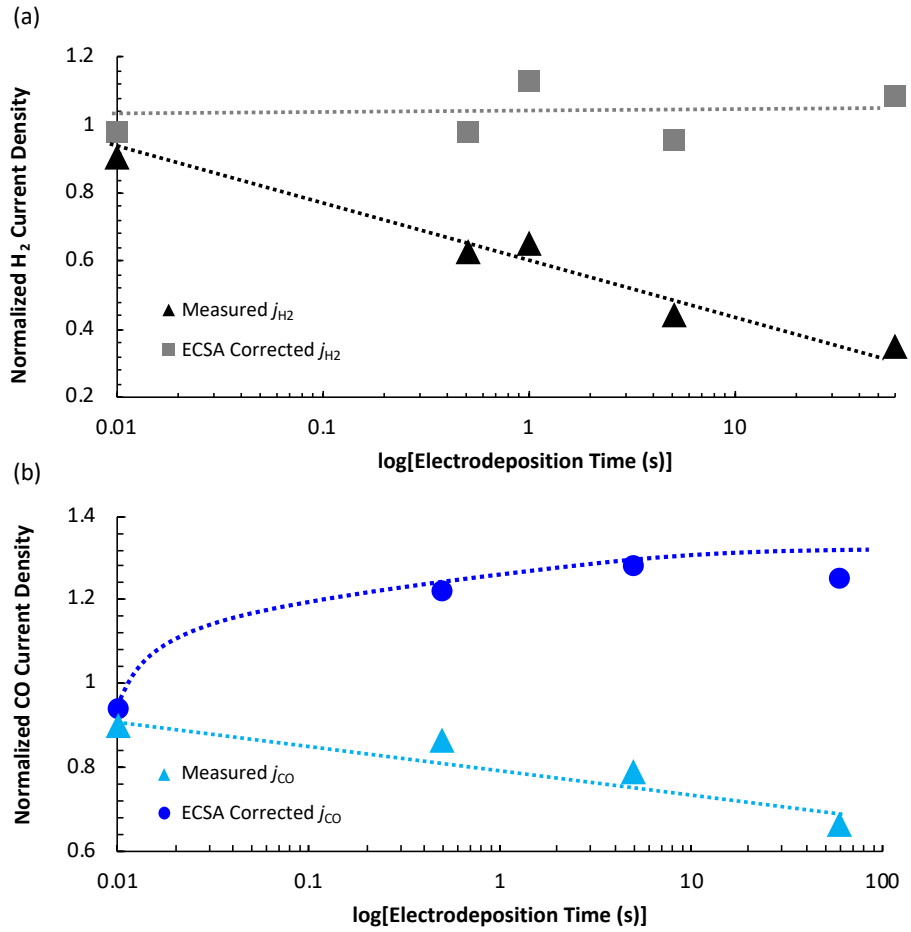

Fig. S19. Plots of normalized partial current densities obtained at −0.9 V vs RHE as a function of the electrodeposition time of **2-Cl**. (a) H_2 (▲ black: measured j_{H2}, ■ grey: corrected j_{H2} by the ECSA). The data suggests that the intrinsic activity of Ag electrodes for HER is not altered by the electrodeposition time of the molecular additive. (b) CO (▲ light blue: measured j_{CO}, ● dark blue: corrected j_{CO} by the ECSA). The data suggests an increase in the intrinsic activity for CO with increased electrodeposition times. This is consistent with the Tafel analysis which indicates improved kinetics for the ET to CO_2 in presence of the organic film. For each experiment, the film was electrodeposited over different time periods (10 ms to 60 sec) at −0.70 V from a 10 mM solution of **2-Cl** dissolved in 0.1 M $KHCO_3$. The dotted lines serve only as a visual guide. Each data point was recorded at least two times to ensure reproducibility.

Table S8. Summary of data recorded for the ECSA and H_2 current density as a function of the electrodeposition time of **2-Cl** for the experiments recorded at –0.9 V.

Time (s)	ECSA (mF/cm^2)			j_{H2} (mA/cm^2)			
	Ag	Ag-2	Normalized	Ag	Ag-2	Intrinsic	Normalized
0.01	7.66E–05	5.02E–05	0.81	–0.76	–0.69	–0.75	0.98
0.5	6.80E–05	4.38E–05	0.64	–1.08	–0.68	–1.06	0.98
1	8.31E–05	4.99E–05	0.61	–1.04	–0.68	–1.11	1.13
5	9.05E–05	4.06E–05	0.46	–0.99	–0.44	–0.95	0.96
60	7.97E–05	2.41E–05	0.31	–0.88	–0.30	–0.96	1.09

Table S9. Summary of data recorded for the ECSA and CO partial current density as a function of the electrodeposition time of **2-Cl** for the experiments recorded at –0.9 V.

Time (s)	ECSA (mF/cm^2)			j_{CO} (mA/cm^2)			
	Ag	Ag-2	Normalized	Ag	Ag-2	Intrinsic	Normalized
0.01	6.20E–05	4.46E–05	0.81	–0.33	–0.29	–0.36	1.09
0.5	5.63E–05	4.07E–05	0.72	–0.36	–0.32	–0.44	1.22
5	6.05E–05	3.85E–05	0.64	–0.42	–0.34	–0.53	1.26
60	5.77E–05	3.14E–05	0.54	–0.40	–0.27	–0.50	1.25

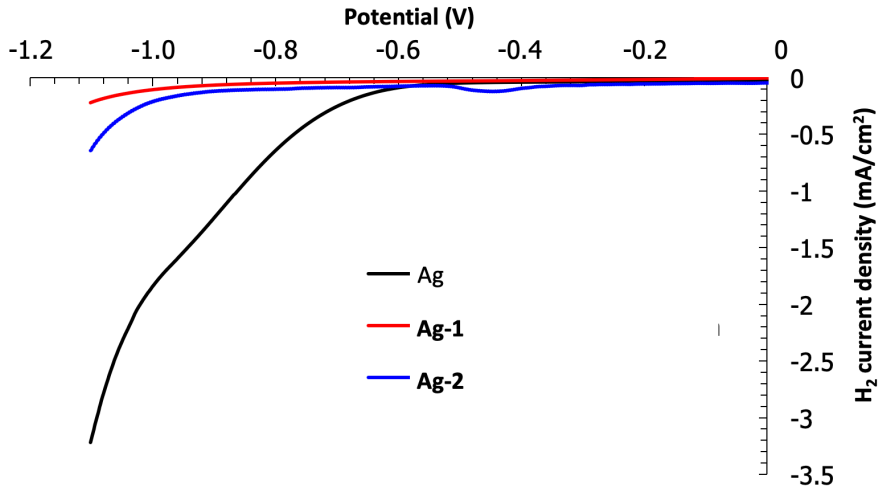

Fig. S19. LSV scans recorded in N_2-saturated 0.1 M $KHCO_3$ from 0 V to –1.1 V for Ag (black trace), **Ag-1** (red trace) and **Ag-2** (blue trace).

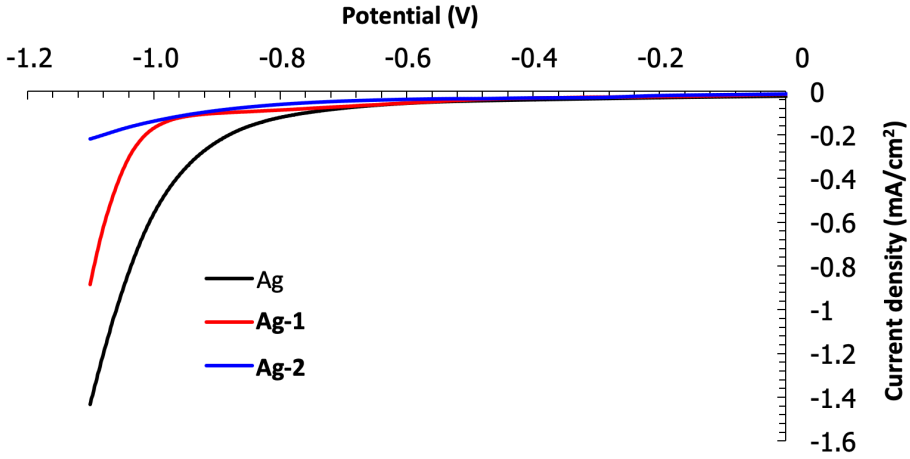

Fig. S20. LSV scan recorded in CO_2-saturated 0.1 M $KHCO_3$ from 0 V to –1.1 V for Ag (black trace), **Ag-1** (red trace) and **Ag-2** (blue trace).

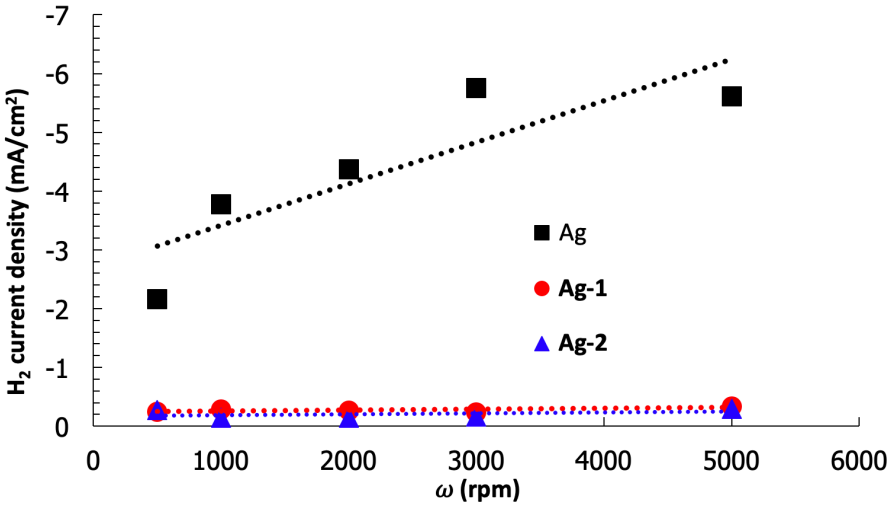

Fig. S21. Plot of the dependence of the rotation rate of the Ag electrode on the HER activity recorded between 500 rpm and 5000 rpm during 35 min of bulk electrocatalysis at –1.1 V in N_2-saturated 0.1 M $KHCO_3$ for Ag (■), **Ag-1** (●) and **Ag-2** (▲).

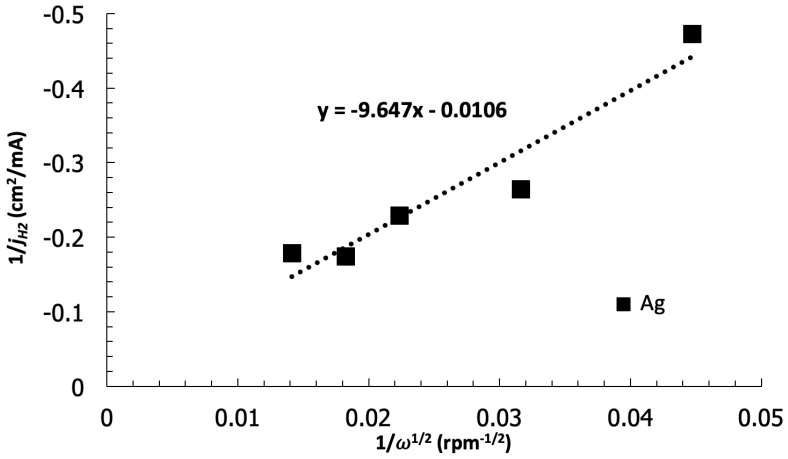

Fig. S22. Koutecky-Levich plot of H_2 partial current density operated in N_2-saturated 0.1 M $KHCO_3$ electrolyte on a rotating Ag disc electrode at –1.1 V.

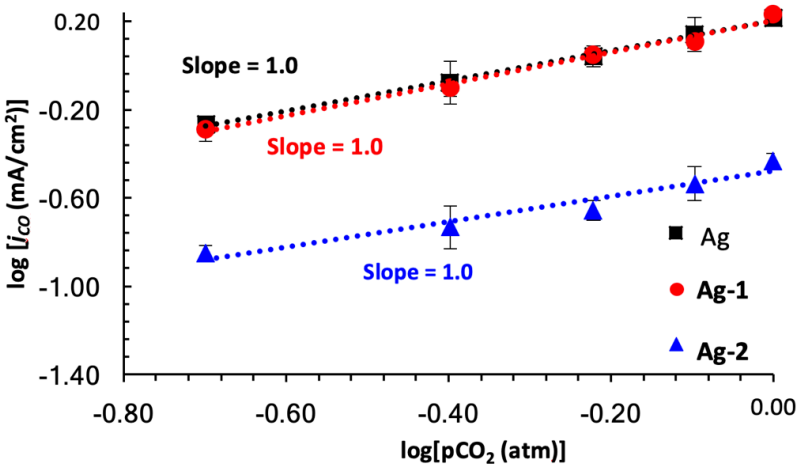

Fig. S23. pCO_2 dependence of the CO current density conducted in 0.1 M $KHCO_3$, at –1.1 V for Ag (■), **Ag-1** (●) and **Ag-2** (▲). The flow of CO_2 was varied between 1 sccm to 5 sccm and N_2 was used as a balance gas to keep a total flow of 5 sccm. The data shows a first order dependence on CO_2 for Ag, **Ag-1** and **Ag-2**.

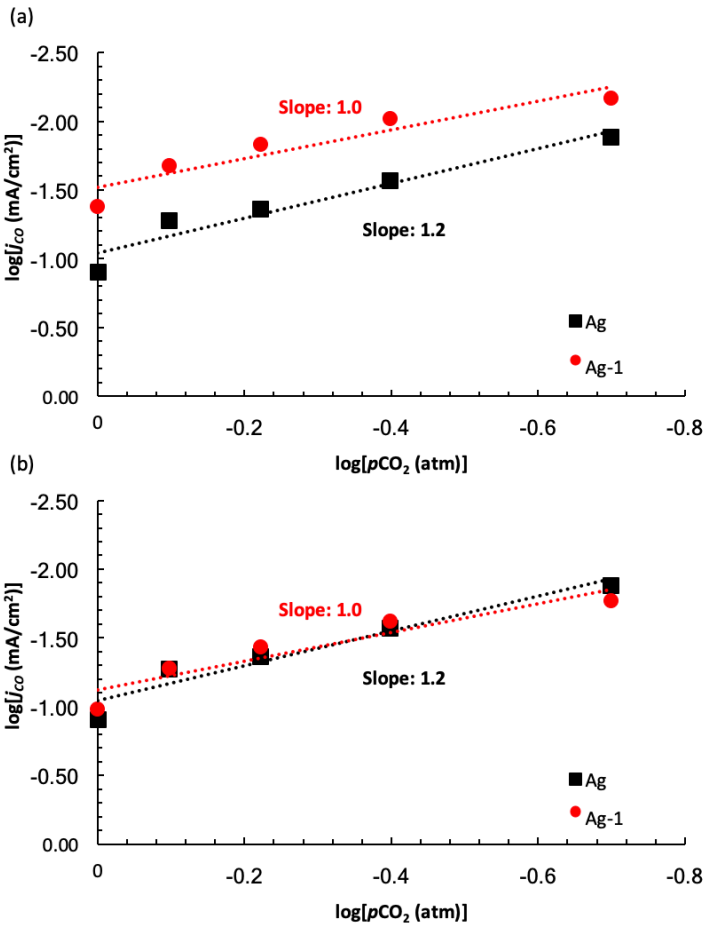

Fig. S24. pCO_2 dependence of the CO current density conducted in 0.1 M $KHCO_3$ (a) before (b) after correction with the ECSA, at –0.9 V for Ag (■) and **Ag-1** (●). The flow of CO_2 was varied between 1 sccm to 5 sccm and N_2 was used as a balance gas to keep a total flow of 5 sccm. The data also shows a first order dependence on CO_2 for Ag, **Ag-1** and similar intrinsic activities suggesting that the diffusion of CO_2 is not limited by the organic film deposited in **Ag-1**.

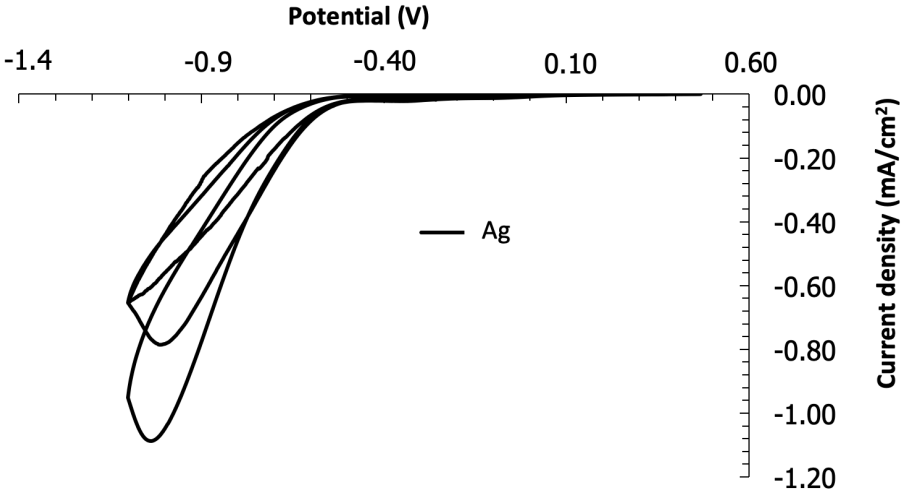

Fig. S25. First three CV scans recorded on Ag electrode from 0.6 V until –1.0 V in CO_2-saturated 0.1 M $KHCO_3$ electrolyte at a scan rate of 20 mV/s.

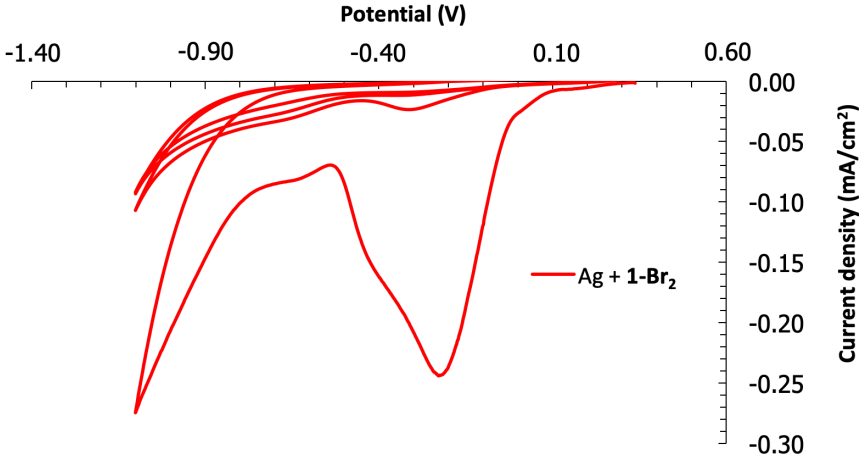

Fig. S26. First four CV scans recorded on Ag electrode from 0.6 V until –1.0 V in CO_2-saturated 0.1 M $KHCO_3$ electrolyte in presence of 10 mM of **1-Br$_2$** at a scan rate of 20 mV/s.

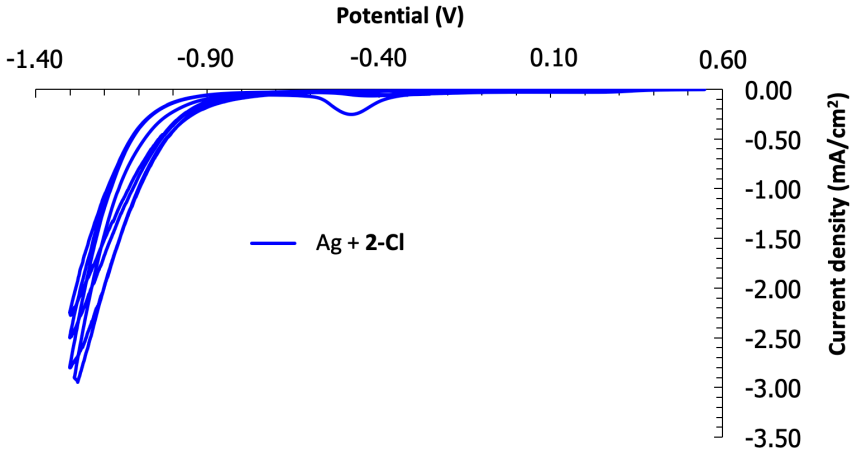

Fig. S27. First four CV scans recorded on Ag electrode from 0.5 V until –1.3 V in CO_2-saturated 0.1 M $KHCO_3$ electrolyte in presence of 10 mM of **1-Cl** at a scan rate of 20 mV/s.

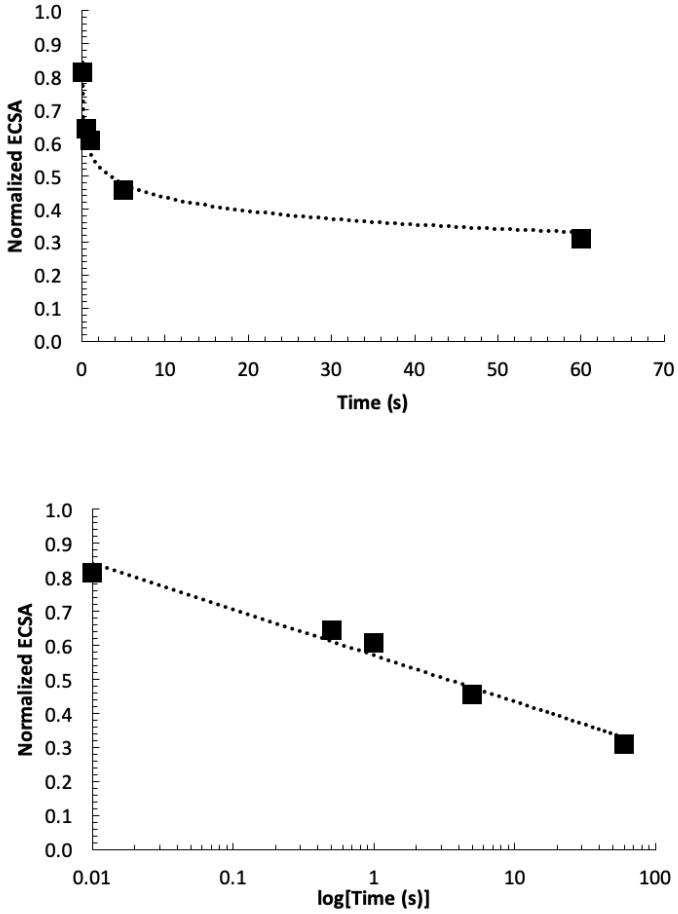

Fig. S28. (a) Correlation between the normalized ECSA area against the electrodeposition time of **2-Cl** under N_2. (b) Same plot but with a logarithmic time scale.

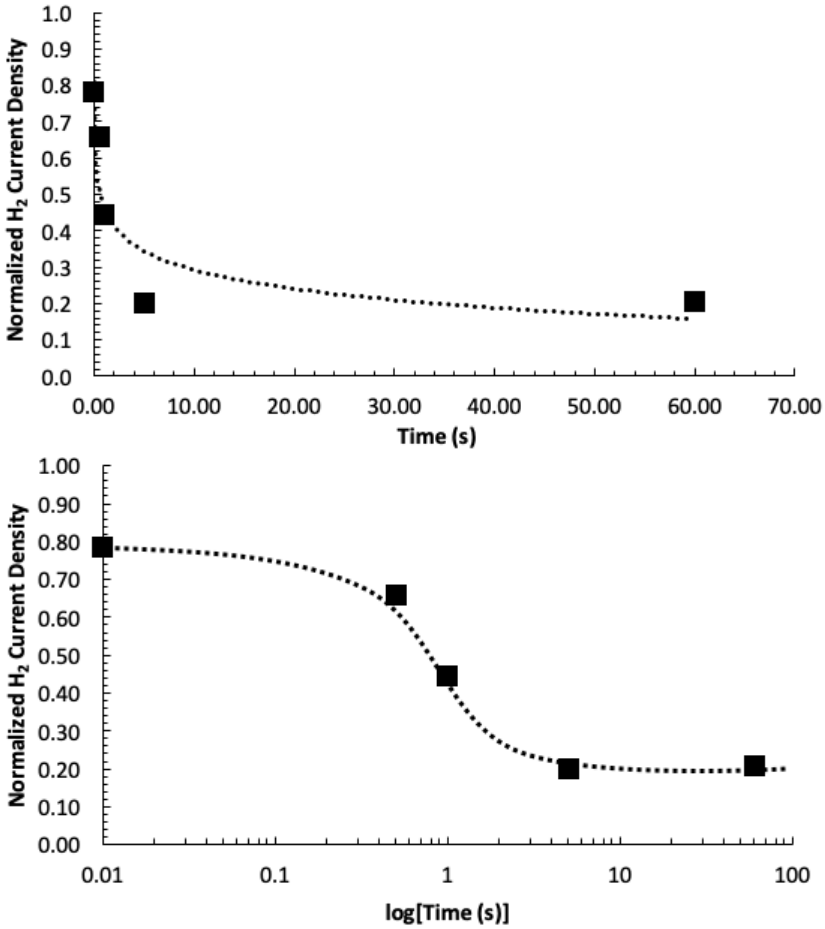

Fig. S29. (a) Plot of the normalized current density for H_2 at –1.1 V against the electrodeposition time of **2-Cl** under N_2. (b) Same plot but with a logarithmic time scale.

Table S10. Summary of data recorded for the ECSA and H_2 current density as a function of the electrodeposition time of **2-Cl** for the experiments recorded at –1.1 V.

Time (s)	ECSA (mF/cm^2)			j_{H2} (mA/cm^2)		
	Ag	**Ag-2**	**Normalized**	**Ag**	**Ag-2**	**Normalized**
0.01	6.39E–05	5.46E–05	0.87	–3.01	–2.34	0.78
0.5	5.49E–05	3.49E–05	0.64	–3.22	–2.12	0.66
1	6.82E–05	4.09E–05	0.61	–2.76	–1.23	0.44
5	6.57E–05	3.57E–05	0.55	–3.19	–0.66	0.20
60	6.97E–05	3.33E–05	0.47	–3.06	–0.62	0.21

Table S11. Summary of data recorded for the ECSA and CO partial current density as a function of the electrodeposition time of **2-Cl** for the experiments recorded at –1.1 V.

Time (s)	ECSA (mF/cm^2)			j_{CO} (mA/cm^2)		
	Ag	Ag-2	Normalized	Ag	Ag-2	Normalized
0.01	1.14E–04	1.12E–04	0.84	–1.65	–1.69	1.03
0.5	1.14E–04	0.99E–04	0.71	–1.58	–2.12	0.91
1	1.14E–04	0.91E–04	0.65	–1.67	–1.22	0.90
5	1.12E–04	0.67E–04	0.53	–1.64	–1.59	0.97
60	1.13E–04	0.56E–04	0.44	–1.69	–1.50	0.88

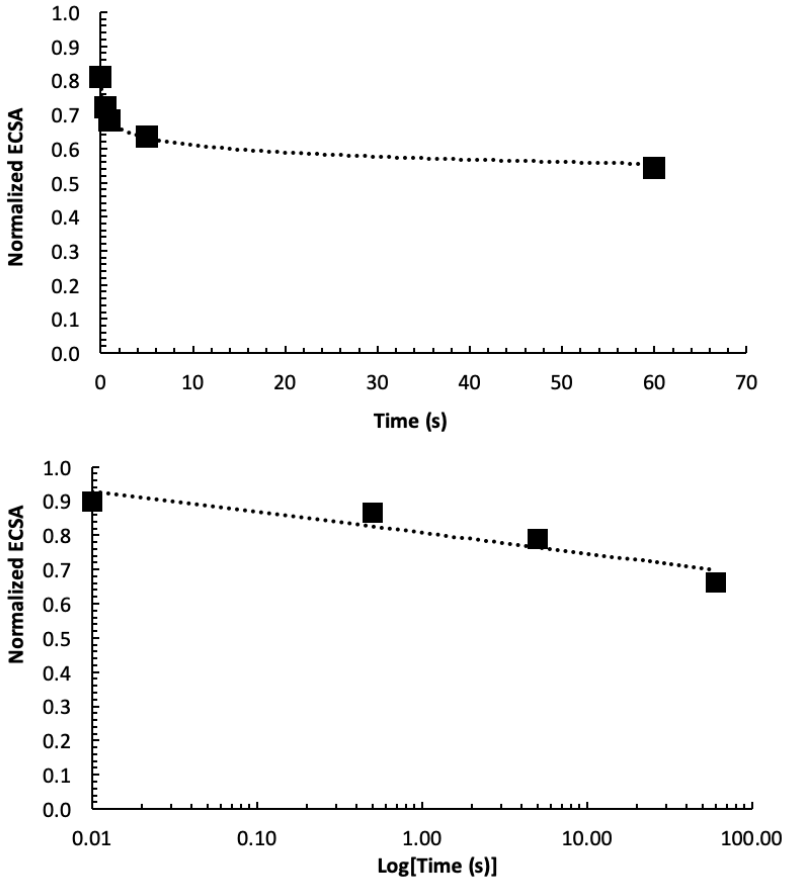

Fig. S30. (a) Plot of the normalized ECSA against the electrodeposition time of **2-Cl** under CO_2. (b) Same plot but with a logarithmic time scale.

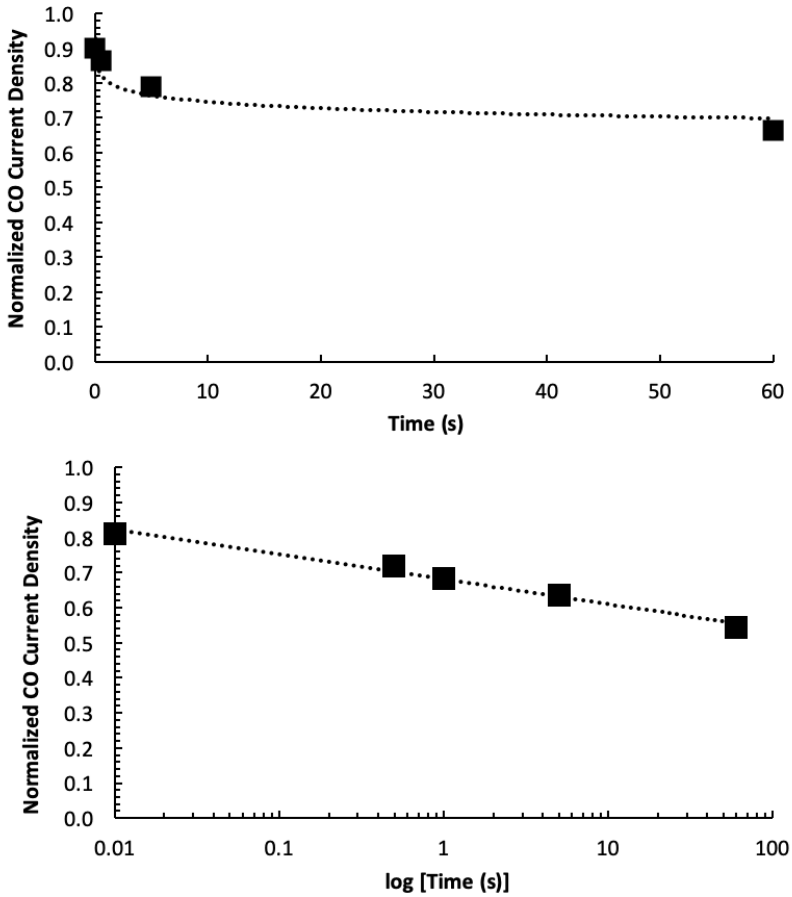

Fig. S31. (a) Plot of the normalized current density for CO at –1.1 V against the electrodeposition time of **2-Cl** under CO_2. (b) Same plot but with a logarithmic time scale.

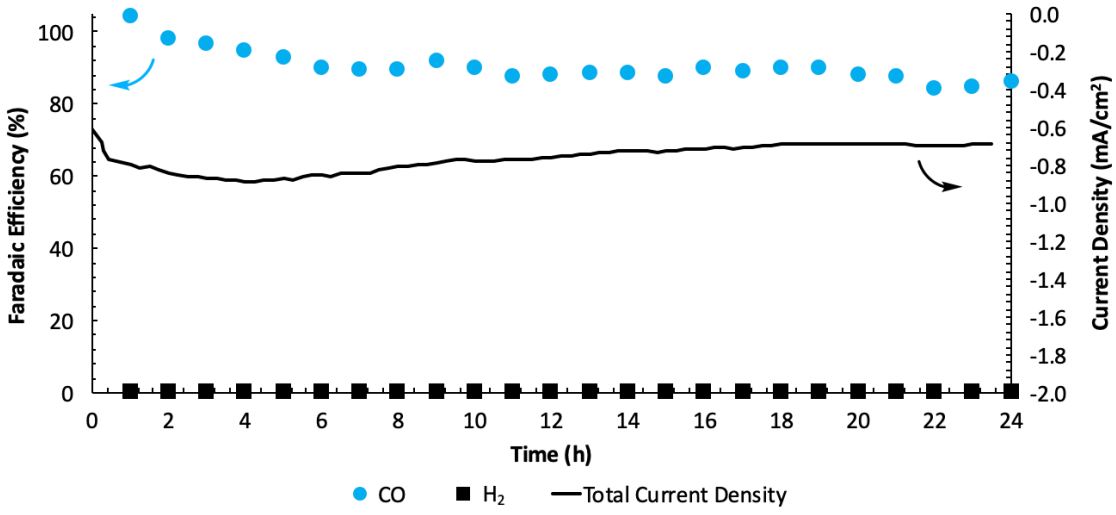

Fig. S32. Evolution of FEs for CO (●) and H_2 (■), and total current density over a 24 h bulk electrolysis on **Ag-1** in a CO_2-saturated 0.1 M $KHCO_3$ electrolyte, without additive, at –1.0 V. **Ag-1** was prepared by bulk electrolysis at -1.0 V for 1 h in a CO_2-saturated 0.1 M $KHCO_3$ electrolyte containing 10 mM of **1-Br₂**. The cathodic chamber was rinsed 3x with fresh electrolyte containing no additive before starting the 24 h run.

References

1. A. Thevenon, A. Rosas-Hernández, J. C. Peters, T. Agapie, In-Situ Nanostructuring and Stabilization of Polycrystalline Copper by an Organic Salt Additive Promotes Electrocatalytic CO_2 Reduction to Ethylene. *Angew. Chem. Int. Ed.* **58**, 16952–16958 (2019).
2. Z. Han, R. Kortlever, H.-Y. Chen, J. C. Peters, T. Agapie, CO_2 Reduction Selective for $C_{\geq 2}$ Products on Polycrystalline Copper with N-Substituted Pyridinium Additives. *ACS Cent. Sci.* **3**, 853–859 (2017).
3. P. Lobaccaro, *et al.*, Effects of temperature and gas–liquid mass transfer on the operation of small electrochemical cells for the quantitative evaluation of CO_2 reduction electrocatalysts. *Phys. Chem. Chem. Phys.* **18**, 26777–26785 (2016).
4. X. Liu, *et al.*, pH effects on the electrochemical reduction of CO_2 towards C_2 products on stepped copper. *Nat. Commun.* **10**, 1–10 (2019).